

# Incomplete remyelination via therapeutically enhanced oligodendrogenesis is sufficient to recover visual cortical function

Received: 20 February 2024

Accepted: 9 January 2025

Published online: 16 January 2025

 Check for updates

A list of authors and their affiliations appears at the end of the paper

Myelin loss induces neural dysfunction and contributes to the pathophysiology of neurodegenerative diseases, injury conditions, and aging. Because remyelination is often incomplete, better understanding endogenous remyelination and developing remyelination therapies that restore neural function are clinical imperatives. Here, we use *in vivo* two-photon microscopy and electrophysiology to study the dynamics of endogenous and therapeutic-induced cortical remyelination and functional recovery after cuprizone-mediated demyelination in mice. We focus on the visual pathway, which is uniquely positioned to provide insights into structure-function relationships during de/remyelination. We show endogenous remyelination is driven by recent oligodendrocyte loss and is highly efficacious following mild demyelination, but fails to restore the oligodendrocyte population when high rates of oligodendrocyte loss occur quickly. Testing a thyromimetic (LL-341070) compared to clemastine, we find it better enhances oligodendrocyte gain and hastens recovery of neuronal function. The therapeutic benefit of the thyromimetic is temporally restricted, and it acts exclusively following moderate to severe demyelination, eliminating the endogenous remyelination deficit. However, we find regeneration of oligodendrocytes and myelin to healthy levels is not necessary for recovery of visual neuronal function. These findings advance our understanding of remyelination and its impact on functional recovery to inform future therapeutic strategies.

Myelin, made by oligodendrocytes enwrapping axons with lipid-rich membranes, is essential for proper central nervous system (CNS) function. Loss of oligodendrocytes and myelin – known as demyelination – induces severe delay and failure of action potential propagation<sup>1,2</sup>, leaves neurons and their axons vulnerable to degeneration<sup>3–5</sup>, and causes motor, sensory, and cognitive impairment<sup>6,7</sup>. Demyelination occurs in white and gray matter in pathologies, including inflammatory demyelinating diseases like multiple sclerosis<sup>8</sup>, traumatic CNS injury<sup>9,10</sup>, stroke<sup>11</sup>, Alzheimer's disease<sup>12</sup>,

and aging<sup>13,14</sup>. In particular, neocortical gray matter demyelination is highly correlated with physical and cognitive disability in multiple sclerosis<sup>15</sup>, emphasizing the clinical importance of understanding the role of neocortical myelin in neuronal function<sup>16</sup>.

Demyelination is typically followed by a period of heightened new myelin formation known as remyelination, which can restore action potential propagation and prevent neurodegeneration<sup>2,4,5</sup>. Remyelination is carried out primarily by newly formed oligodendrocytes differentiating from parenchymal and germinal zone derived

✉ e-mail: [daniel.denman@cuanschutz.edu](mailto:daniel.denman@cuanschutz.edu); [ethan.hughes@cuanschutz.edu](mailto:ethan.hughes@cuanschutz.edu)

oligodendrocyte precursor cells (OPCs)<sup>17–20</sup> as well as – in some instances – by oligodendrocytes that survive the demyelinating injury<sup>21–24</sup>. However, the endogenous remyelination response is often incomplete, resulting in chronic demyelination<sup>25,26</sup> and limited functional recovery<sup>27,28</sup>. Thus, understanding the drivers and limitations of endogenous remyelination and developing methods to enhance it are clinical imperatives for many demyelinating conditions. Despite substantial progress in identifying compounds that improve remyelination in recent years, there is still no FDA-approved remyelination therapy. Furthermore, independent of specific therapeutic strategies, we require a deeper understanding of fundamental aspects of therapeutic-induced remyelination, such as the dynamics and constraints of therapeutic action, and the magnitude and timing of remyelination required to recover neuronal function.

The afferent visual pathway is well-suited to investigate the relationship between myelin and neuronal function throughout de/remyelination<sup>29</sup>. The circuits of primary visual cortex (V1) are sensitive to input spike precision<sup>30</sup> and contain precise and reliable sensory-evoked activity<sup>31–33</sup>, important for action potential transmission and visual coding<sup>34,35</sup>. Moreover, perturbations in the timing of sensory-evoked activity in V1 have previously been observed in patients and animal models during de/remyelination<sup>27,36–38</sup>. Here, we used longitudinal in vivo two-photon imaging of oligodendrocytes and high-density electrical recordings with single neuron resolution in V1 to study the dynamics of endogenous and therapeutic-induced neocortical remyelination and the relationship between remyelination and functional recovery. Demyelination was induced with cuprizone, and mice were treated with two remyelination drugs: a new thyroid hormone mimetic (thyromimetic), LL-341070, and a clinically validated therapeutic, clemastine<sup>37</sup>.

Cuprizone treatment induced oligodendrocyte loss and a concomitant increase in visual response latency. This was followed by a rapid and robust endogenous remyelination response that was driven by recent oligodendrocyte loss. Endogenous remyelination was highly efficacious at mild demyelination levels, but when moderate or severe demyelination occurred quickly, endogenous remyelination failed to restore the oligodendrocyte population after seven weeks. Treatment with a high dose of LL-341070 substantially increased regenerative oligodendrogenesis during remyelination, acting more quickly and robustly than clemastine, and hastened neuron functional recovery. The therapeutic benefit of LL-341070 was loss-dependent, exclusively impacting remyelination after moderate or severe demyelination. Consequently, LL-341070 eliminated the endogenous remyelination deficit after seven weeks of remyelination, restoring oligodendrocyte numbers to original levels and myelin to levels comparable to those of age-matched healthy mice. However, full restoration of oligodendrocytes and myelin to these levels was not necessary to recover neuronal function.

## Results

### Severity of demyelination determines the extent of oligodendrocyte regeneration

To induce demyelination, 9–10-week-old mice were fed chow containing 0.2% cuprizone. Cuprizone is a copper chelator widely used to cause specific oligodendrocyte cell death and demyelination, although its mechanism of action is incompletely understood<sup>39,40</sup>. After a subacute exposure (3.5 weeks versus commonly used exposure of 6 weeks<sup>40</sup>), mice were returned to their normal diet for seven additional weeks to allow for remyelination (Fig. 1A). Using histology, we did not find evidence of demyelination in the visual thalamus or optic nerve (Supplementary Fig. 1A–H), but we detected significant oligodendrocyte loss in V1 and the subadjacent optic radiation (Supplementary Fig. 1I–L), indicating demyelination is specifically targeted to the posterior visual pathway in this cuprizone exposure protocol. Importantly, we did not observe loss of retinal ganglion cells in the

retina or damage to axons in V1 or optic radiation (Supplementary Fig. 2), reflecting preservation of neuronal and axonal health.

To examine the dynamics of cortical demyelination, we used longitudinal in vivo two-photon imaging of V1 in *Mobp-EGFP* mice (Fig. 1B, C). These mice express *EGFP* under the promoter/enhancer for myelin-associated oligodendrocyte basic protein (*Mobp*), specifically labeling all oligodendrocytes and their associated myelin sheaths with *EGFP* (Fig. 1D)<sup>41</sup>. In vivo imaging throughout this period enabled the longitudinal tracking of oligodendrocytes in individual mice over time (Fig. 1A, D, E). Since we did not observe differences between untreated animals and mice treated with different vehicles used in this study (Supplementary Fig. 3), we combined these groups to investigate endogenous remyelination.

Cuprizone treatment resulted in overlapping periods of oligodendrocyte loss and gain (Fig. 1D, E) with sigmoidal dynamics that were well modeled by three parameter Gompertz growth curves (Fig. 1F and Supplementary Fig. 4A, B), allowing us to derive cumulative loss and gain asymptotes and timing of maximum rates (Fig. 1F). Oligodendrocyte loss began during the cuprizone period and plateaued approximately three weeks following cuprizone removal, with a maximum loss rate  $2 \pm 0.6$  (mean  $\pm$  SEM) days prior to cuprizone removal (Fig. 1E, F, and Supplementary Fig. 4A, D). Oligodendrocyte gain was suppressed during cuprizone and began to increase in rate at the end of cuprizone treatment (Fig. 1E, F, and Supplementary Fig. 4B, E). Oligodendrocyte gain rate peaked  $11 \pm 0.9$  (mean  $\pm$  SEM) days after cuprizone removal, significantly later than loss (Fig. 1F). Between individual mice, we observed a large range in the extent of oligodendrocyte loss in the visual cortex (14% to 80% at 3 weeks) (Fig. 1E and Supplementary 4A), which was tightly positively correlated with the magnitude and rate of oligodendrocyte gain throughout remyelination (Fig. 1G and Supplementary Fig. 5A–E). However, the relationship between the magnitude of oligodendrocyte loss and gain was not one-to-one (Fig. 1G). Oligodendrocyte gain was insufficient to replace all lost oligodendrocytes by seven weeks of remyelination (Fig. 1F), consistent with findings in other cortical regions following cuprizone<sup>21,42</sup>. Interestingly, this deficit in endogenous cortical remyelination depended on the magnitude of oligodendrocyte loss incurred. Mice that lost fewer than 50% of oligodendrocytes generated as many new oligodendrocytes by seven weeks as they had lost, while mice that lost greater than 50% of oligodendrocytes failed to gain sufficient numbers of new oligodendrocytes to replace them (Fig. 1H). Thus, by seven weeks, there was a strong negative correlation between oligodendrocyte loss magnitude and oligodendrocyte number, with only mice with low levels of oligodendrocyte loss regenerating their original oligodendrocyte population while mice with high levels of oligodendrocyte loss exhibited a regeneration deficit (Fig. 1I, J). It is likely that this regeneration gap between mice incurring low and high levels of oligodendrocyte loss will persist since oligodendrocyte gain rate was no longer correlated with oligodendrocyte loss magnitude by seven weeks of remyelination (Supplementary Fig. 5F). Assuming rates of oligodendrocyte gain from five to seven weeks are maintained indefinitely, it would take an additional 19.6 weeks (overall mouse age would be ~9 months old) for mice with 75% loss and 25% loss to have equal numbers of oligodendrocytes (Supplementary Table 1). However, it is unlikely that oligodendrocyte gain rates will sustain these levels as oligodendrogenesis decreases radically with aging<sup>43</sup>; thus, the regeneration gap between mice incurring high and low oligodendrocyte loss will likely persist even past this point.

### Oligodendrocyte gain during remyelination is driven by recent oligodendrocyte loss

Elevated oligodendrocyte gain rates in response to oligodendrocyte loss is widely observed in animal models of demyelination (Supplementary Fig. 4E)<sup>13,21,24,42,44,45</sup>. Yet, we have a limited understanding of the factors initiating this endogenous response. Elevated gain rates

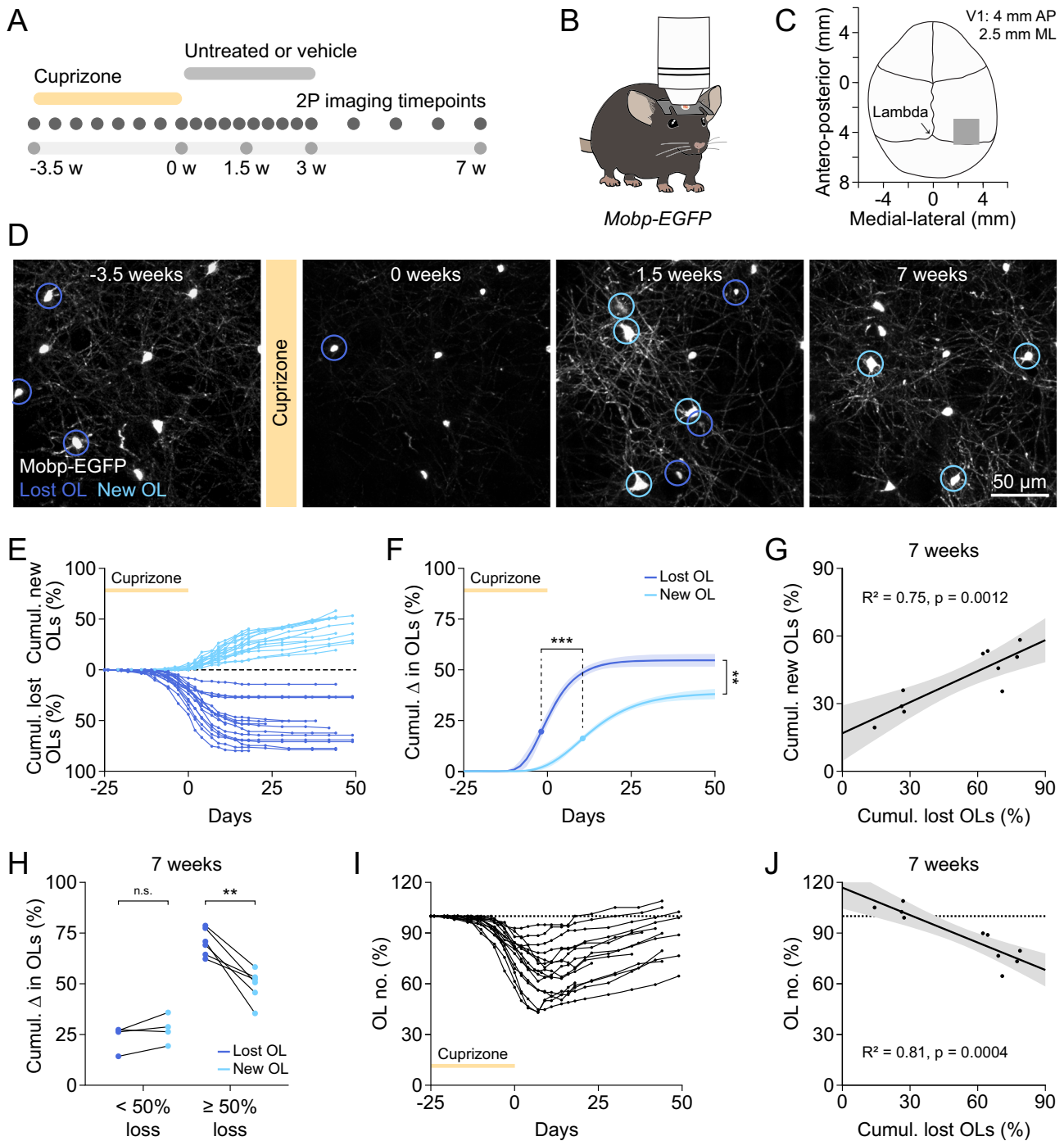


**Fig. 1 | Endogenous remyelination fails to restore the oligodendrocyte population after moderate or severe demyelination.** **A** Experimental timeline. Untreated and vehicle-treated mice were used to study endogenous remyelination. **B** *Mbp-EGFP* mice underwent longitudinal in vivo two-photon imaging of OLs in V1. **C** Cranial window placement above V1. **D** Representative images of V1 OLs in one mouse at baseline (-3.5 weeks), end of cuprizone (0 weeks), and during remyelination (1.5 and 7 weeks). Lost OLs (dark blue) and new OLs (light blue) are encircled. **E** Cumulative OL loss and gain (as a percentage of baseline OLs) in individual mice over time ( $n = 15$ ). **F** Three parameter Gompertz growth curve (95% CI) fit to group cumulative OL loss and gain shown for visualization. Statistical comparisons performed on parameters derived from three parameter growth curves fit to individual mice (Supplementary Fig. 4A, B). Maximum growth rate occurred earlier for loss than gain. Gain asymptote is lower than loss

asymptote. **G** Cumulative OL gain and cumulative OL loss are tightly correlated at 7 weeks. **H** At <50% OL loss, mice make as many new OLs as they lose by 7 weeks. At  $\geq 50\%$  OL loss, mice make fewer new OLs than they lose. **I** OL number (as a percentage of baseline OLs) in individual mice over time ( $n = 15$ ). Dashed line at 100%. **J** OL number and cumulative OL loss are tightly correlated at 7 weeks. In (F), Max. growth rate: paired t test ( $t(14) = 10.12$ ,  $***p < 0.0001$ ,  $n = 15$ ). Asymptote: paired t test ( $t(14) = 3.64$ ,  $**p = 0.0027$ ,  $n = 15$ ). In (G), linear regression ( $F(1, 8) = 23.79$ ,  $n = 10$ ). In (H) <50% loss, paired t test ( $t(3) = 1.87$ ,  $p = 0.16$ ,  $n = 4$ ). In  $\geq 50\%$  loss, paired t test ( $t(5) = 5.40$ ,  $**p = 0.0029$ ,  $n = 6$ ). In (J), linear regression ( $F(1, 8) = 33.06$ ,  $n = 10$ ). n.s. not significant,  $**p < 0.01$ ,  $***p < 0.001$ ; line of best fit  $\pm$  95% CI in (G, J); n=mice; two-sided statistical tests. See Supplementary Data 1 for statistical details and Source Data file for source data. OL = oligodendrocyte, V1 = primary visual cortex.

correlate with loss levels (Supplementary Fig. 5C–E) and subside shortly following the end of loss (Supplementary Fig. 4E), indicating both a scale and temporal dependence of oligodendrocyte gain on loss. However, it is unknown whether oligodendrocyte gain is induced in response to (a) a reduction in oligodendrocyte number initiating a homeostatic-like drive to restore the population, and/or (b) acute signaling around the loss of oligodendrocytes. Exploiting the lengthy, overlapping periods of oligodendrocyte loss and gain with varying levels between mice (Fig. 1E), we tested which parameters best predicted oligodendrocyte gain rate during remyelination. We modeled our longitudinal data to assess parameters continuously (Supplementary Fig. 4A–E).

If restoration of the oligodendrocyte population drives oligodendrocyte gain rate, we would expect gain rate to be higher the further oligodendrocyte numbers are from pre-cuprizone levels. To test this, we assessed the correlation between oligodendrocyte number and gain rate (Fig. 2A, B). We found that oligodendrocyte gain rate at 14 days post-cuprizone was weakly predicted by oligodendrocyte number at 7 days post-cuprizone (Fig. 2A). In assessing oligodendrocyte gain rate at 7, 14, 21, and 28 days post-cuprizone, we found that there was no period at which oligodendrocyte number predicted oligodendrocyte gain rate (Fig. 2B), indicating that a drive to reestablish oligodendrocyte numbers is not a primary factor in inducing oligodendrocyte gain during remyelination.

By contrast, cumulative oligodendrocyte loss was more strongly predictive of oligodendrocyte gain rate (Fig. 2C, D). Cumulative oligodendrocyte loss at 7 days post-cuprizone predicted oligodendrocyte gain rate at 14 days post-cuprizone (Fig. 2C). More broadly, cumulative loss throughout the remyelination period was predictive of oligodendrocyte gain rate at several time points (Fig. 2D). Thus, oligodendrocyte gain rate is more responsive to the loss of oligodendrocytes than to oligodendrocyte number.

However, we observed that cumulative loss of oligodendrocytes up until the end of cuprizone treatment (49% of total loss) did not predict oligodendrocyte gain rate at any point during remyelination (Fig. 2D), suggesting that the timing of oligodendrocyte loss was an important factor in the ability to induce future oligodendrocyte gain. To specifically test this, we assessed the correlation between oligodendrocyte loss rate and oligodendrocyte gain rate (Fig. 2E, F). We found that the best predictor of oligodendrocyte gain rate at any time point was the oligodendrocyte loss rate approximately seven days prior (Fig. 2E–G). Oligodendrocyte gain rates at 7, 14, 21, and 28 days were best predicted by the oligodendrocyte loss rates at 4, 7, 14, and 21 days, respectively, and were poorly predicted by loss rates at other time points (Fig. 2E, F). For example, while the oligodendrocyte loss rate at 7 days strongly predicted the oligodendrocyte gain rate at 14 days, it did not predict the oligodendrocyte gain rate at 28 days (Fig. 2E, F). Similarly, the oligodendrocyte loss rate at 21 days strongly predicted the gain rate at 28 days but did not predict the gain rate at 7 days (Fig. 2F). These data support the existence of acute signaling that occurs around the time of oligodendrocyte loss that induces new oligodendrocyte formation approximately one week later (Fig. 2G). Thus, recent oligodendrocyte loss – not oligodendrocyte population restoration – drives a temporally limited endogenous remyelination response.

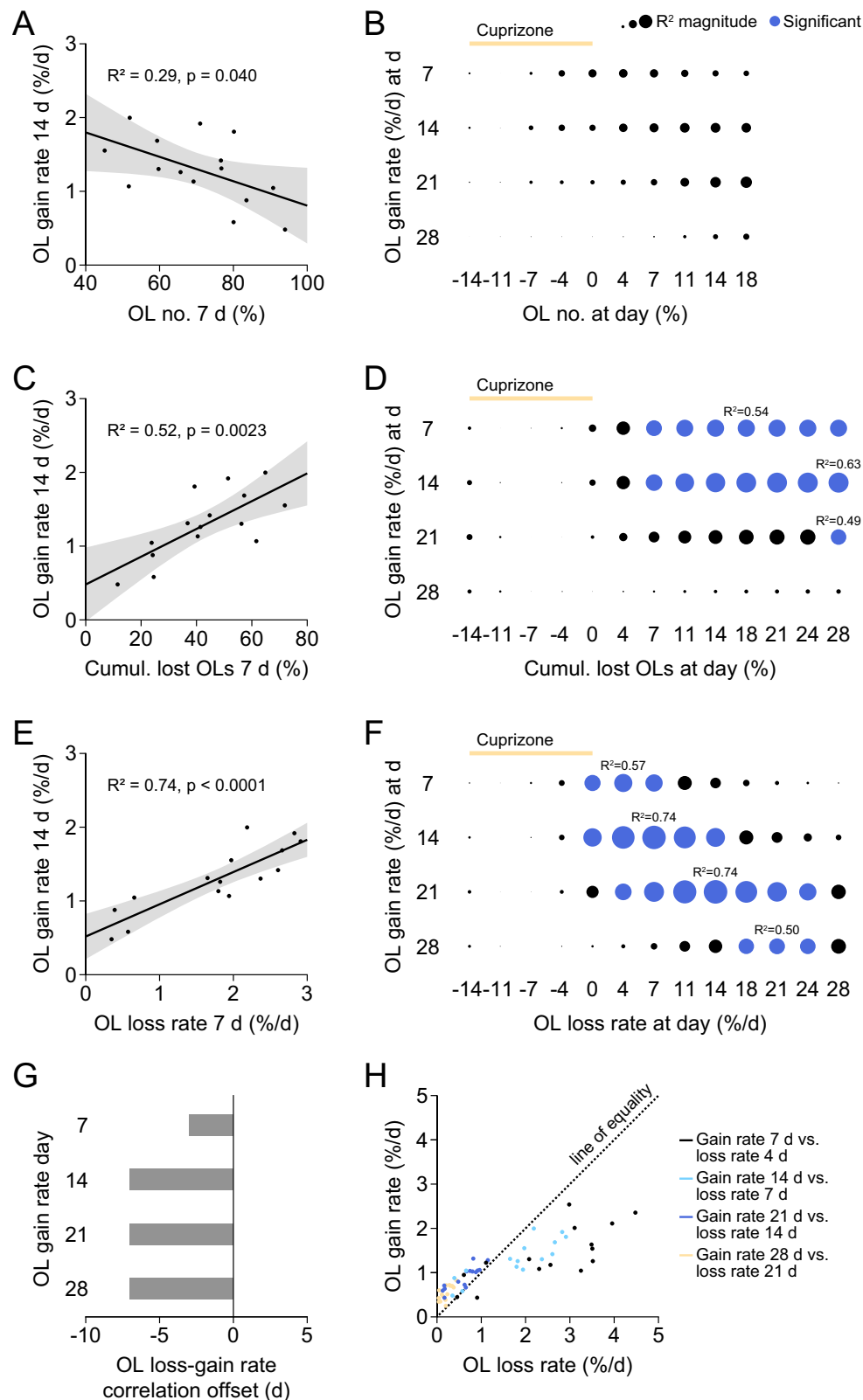
Similar to cumulative oligodendrocyte loss and gain (Fig. 1G), we noticed that the relationship between oligodendrocyte loss rate at 7 days and gain rate at 14 days was not one-to-one (Fig. 2E). Thus, we next sought to determine how the scale of this relationship varied across the magnitude of oligodendrocyte loss or the phase of remyelination. To do this, we plotted oligodendrocyte gain rate at 7, 14, 21, and 28 days versus oligodendrocyte loss rate at 4, 7, 14, and 21 days, respectively (Fig. 2H). At low rates of oligodendrocyte loss (below approximately 1.5% per day), oligodendrocyte gain rate equaled or exceeded the rate of loss (Fig. 2H), regardless of the phase of

remyelination (Fig. 2H). By contrast, at high rates of oligodendrocyte loss (greater than 1.5% per day), which subsided approximately 1.5 weeks post-cuprizone (Supplementary Fig. 4D), oligodendrocyte gain rate could not keep up, never exceeding approximately 2.5% per day despite substantially higher loss rates (Fig. 2H and Supplementary Fig. 4E). Thus, while oligodendrocyte gain during remyelination is induced by recent oligodendrocyte loss, the number of new oligodendrocytes formed per lost oligodendrocyte depends on the rate at which the oligodendrocytes were lost.

### Thyromimetic treatment enhances oligodendrocyte gain during remyelination

Given the limited magnitude (Fig. 1F, H–J) and period (Fig. 2E, F) of endogenous remyelination and the overwhelming presence of chronically demyelinated lesions in multiple sclerosis patients<sup>26,46,47</sup>, identifying exogenous methods to enhance remyelination is a clinical imperative. Thus, we sought to evaluate the ability of a newly developed thyroid hormone receptor beta (TR $\beta$ ) agonist (the thyromimetic LL-341070), to improve oligodendrocyte gain during remyelination. Thyroid hormone and TR $\beta$  agonists are potent inducers of OPC differentiation<sup>48–50</sup> and enhancers of remyelination<sup>51–55</sup>, but their use as remyelination therapeutics has been precluded by peripheral side effects. However, the development of fatty acid amide hydrolase (FAAH)-targeted prodrugs has enabled preferential delivery of systemic doses to CNS tissues<sup>56</sup>. LL-341070 enters the central nervous system as an inactive prodrug, where it is hydrolyzed into its active form by FAAH and is thus able to act locally on TR $\beta$  receptors (Fig. 3A). Initial characterization confirmed the increased selectivity of the active LL-341070 drug to TR $\beta$ , and its ability to induce OPC differentiation in vitro and thyroid hormone target gene expression in vivo (Supplementary Fig. 6A–H), prompting us to evaluate LL-341070 in our model. Following 3.5 weeks of 0.2% cuprizone administration, *Mobp-EGFP* mice were treated daily for the first three weeks of remyelination with 0.3 mg/kg or 0.1 mg/kg LL-341070 or vehicle (Fig. 3B, C). Mice underwent longitudinal in vivo two-photon imaging of VI to allow for tracking of oligodendrocyte loss and gain throughout the demyelination and remyelination periods (Fig. 3B, D–F, and Supplementary Fig. 7).

As observed in control mice (Fig. 1E), all groups experienced a range in the level of oligodendrocyte loss (Fig. 3D, E). However, there was no difference in the mean or variance between groups (Fig. 3E), indicating LL-341070 does not protect oligodendrocytes from death as other thyromimetics have been shown to do in other models<sup>57</sup>. Since oligodendrocyte gain is proportional to loss (Fig. 1G and Supplementary Fig. 5A, B), it was important to account for the level of loss incurred by each mouse when testing the role of thyromimetic treatment on oligodendrocyte gain. To do this, we used an analysis of covariance with unequal slopes to test the effect of treatment on cumulative oligodendrocyte gain while considering the effect of cumulative oligodendrocyte loss and the interaction between cumulative oligodendrocyte loss and treatment (see *Statistics and modeling* in Methods) (Fig. 3G and Supplementary Fig. 8A, B). At 1.5 weeks, we found a significant effect of treatment, cumulative oligodendrocyte loss, and the interaction of cumulative oligodendrocyte loss and treatment on cumulative oligodendrocyte gain (Fig. 3G). To further investigate the effect of treatment, we used post-hoc Tukey's HSD to determine differences between the treatment groups. We compared the means of cumulative oligodendrocyte gain for each treatment group corrected by cumulative oligodendrocyte loss (least square means) at the overall average level of loss (Fig. 3H). We found that mice treated with the high dose of LL-341070 gained substantially more new oligodendrocytes by 1.5 weeks as compared to mice treated with the low dose or vehicle (Fig. 3F, H, and Supplementary Fig. 7). At the end of drug treatment (three weeks of remyelination), mice treated with the high dose of LL-341070 had a trend of more new oligodendrocytes



than mice treated with vehicle (Fig. 3H). By 7 weeks, mice treated with the low dose of LL-341070 had gained substantially more new oligodendrocytes than vehicle-treated mice and a similar trend was observed for the high dose LL-341070, but the differences did not reach statistical significance (Fig. 3H). Thus, thyromimetic treatment enhances oligodendrocyte gain during remyelination. Gross changes in astrocytes or microglia were not apparent after LL-341070

treatment (Supplementary Fig. 9), though effects not captured by our analyses are possible.

Given the failure of endogenous remyelination to surpass an oligodendrocyte gain rate of approximately 2.5% per day (Fig. 2H and Supplementary Fig. 4E), we next sought to understand how thyromimetic treatment impacted oligodendrocyte gain rate. Like cumulative oligodendrocyte gain, oligodendrocyte gain rate

**Fig. 2 | Endogenous remyelination is driven by recent oligodendrocyte loss.** **A, C, E** OL gain rate (as a percentage of baseline OLs per day) at 14 days is weakly correlated with OL number (as a percentage of baseline OLs) at 7 days (**A**), correlated with cumulative OL loss (as a percentage of baseline OLs) at 7 days (**C**), and strongly correlated with OL loss rate (as a percentage of baseline OLs per day) at 7 days (**E**). **B, D, F** OL gain rate at 7, 14, 21, or 28 days does not correlate well with OL number at -14, -11, -7, 0, 4, 7, 11, 14, or 18 days (**B**), correlates well with cumulative OL loss at several days during remyelination (**D**), and correlates best with OL loss rate approximately 7 days prior (**F**). Dot size represents  $R^2$  magnitude.  $R^2$  value is indicated for the strongest significant correlation. Dark blue dots signify significant

correlations (linear regression,  $n = 15$ ) given Bonferroni correction for multiple comparisons,  $p < 0.05/10 = 0.005$  (**B**) or  $p < 0.05/13 = 0.0038$  (**D, F**). **G** OL gain rate at 7, 14, 21, and 28 days is best predicted by OL loss rate 4, 7, 7, and 7 days prior, respectively. **H** Plot of strongest correlations from (F): OL gain rate at 7, 14, 21, and 28 days vs. OL loss rate at 4, 7, 14, and 21 days, respectively (black, light blue, dark blue, yellow, respectively). Dashed line of equality. In (**A**), linear regression ( $F(1, 13) = 5.22$ ,  $n = 15$ ). In (**C**), linear regression ( $F(1, 13) = 14.24$ ,  $n = 15$ ). In (**E**), linear regression ( $F(1, 13) = 37.20$ ,  $n = 15$ ). Line of best fit  $\pm$  95% CI in (**A, C, E**);  $n =$  mice. See Supplementary Data 1 for statistical details and Source Data file for source data. OL = oligodendrocyte.

depends on oligodendrocyte loss (Fig. 2C, D and Supplementary Fig. 5C–E); thus, an analysis of covariance with unequal slopes was used in the same manner to isolate the effects of treatment on oligodendrocyte gain rate. We found that the high dose of LL-341070 increased the maximum oligodendrocyte gain rate during remyelination by two-fold (Fig. 3I and Supplementary Fig. 8C–E). On average, mice treated with the high dose of LL-341070 had a maximum gain rate of  $3.2 \pm 0.35$  (SEM) % per day, with multiple mice exceeding the observed endogenous limit of 2.5% per day (Fig. 3I, Supplementary Fig. 8D, E).

Next, to understand the dynamics with which thyromimetic treatment impacted oligodendrocyte gain, we analyzed oligodendrocyte gain rate across different phases of remyelination. We found that the high dose of LL-341070 increased oligodendrocyte gain rate specifically during the first 1.5 weeks of its administration (Fig. 3J and Supplementary Fig. 8F). Unexpectedly, during the second half of treatment (1.5–3 weeks) or following treatment (3–5 weeks), there was no impact of high dose LL-341070 on oligodendrocyte gain rate (Fig. 3J and Supplementary Fig. 8G, H). Thus, thyromimetic treatment accelerates oligodendrocyte gain during remyelination by transiently increasing oligodendrocyte gain rate during the first half of treatment.

### Severity of demyelination determines efficacy of remyelination therapy

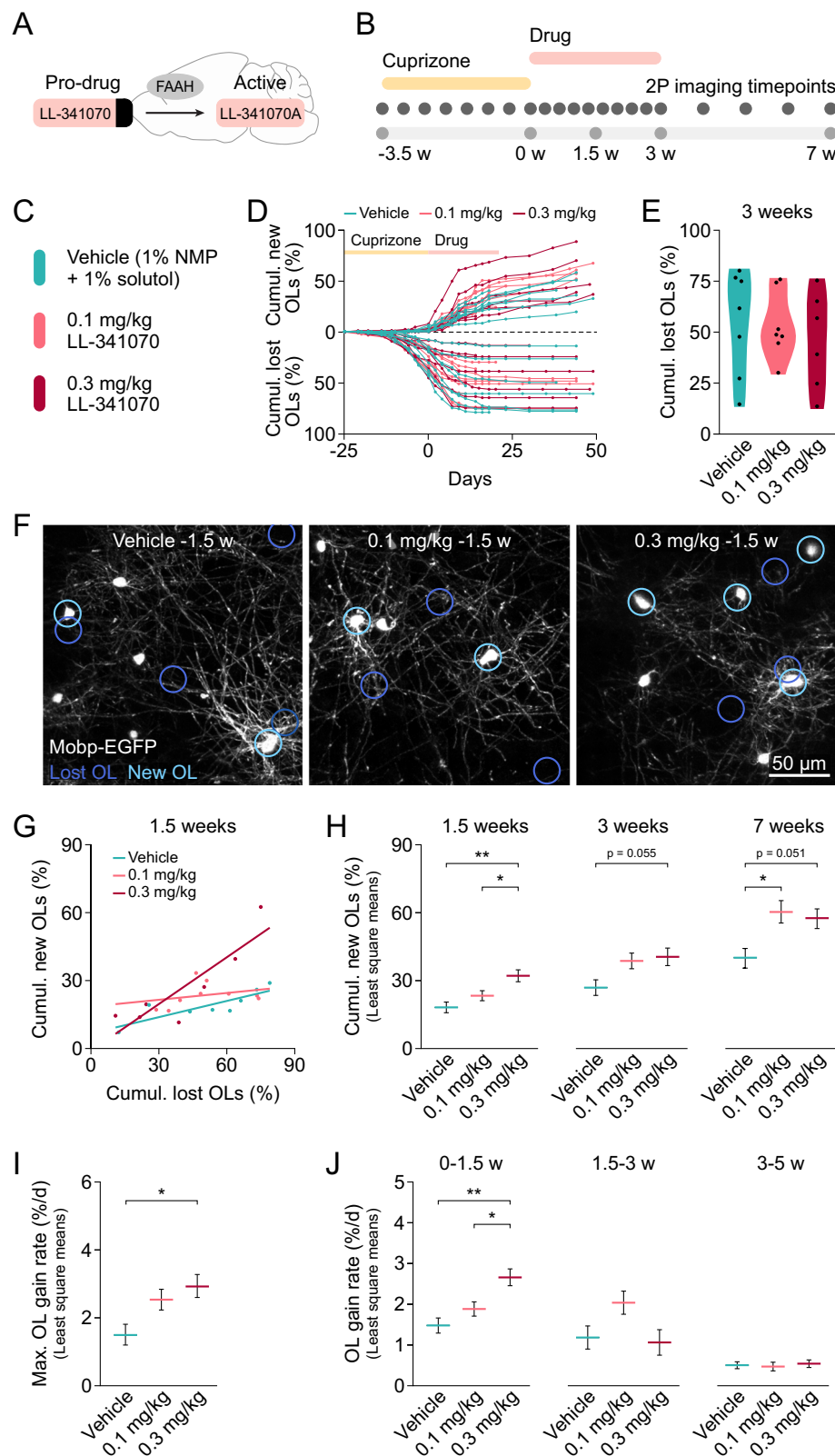
In our analysis of covariance with unequal slopes, we found that the effect of treatment on cumulative oligodendrocyte gain was significantly modulated by the level of cumulative oligodendrocyte loss (i.e. we observed a statistically significant interaction term) (Fig. 3G and Supplementary Data 1). To further dissect this finding, we assessed the ability of thyromimetic treatment to augment cumulative oligodendrocyte gain at low and high levels of cumulative oligodendrocyte loss by subdividing our data into mice that lost more and less than 50% of oligodendrocytes. We found that at less than 50% oligodendrocyte loss, LL-341070 treatment had no impact on cumulative oligodendrocyte gain by 1.5 weeks (Fig. 4A), while in mice with more than 50% oligodendrocyte loss, the high dose of LL-341070 doubled the amount of oligodendrocyte gain (Fig. 4A).

Given this preferential improvement of remyelination at high loss levels, we sought to determine whether thyromimetic treatment would ameliorate the regeneration deficit observed at high loss levels in control mice (Fig. 1H–J). Unlike vehicle-treated mice, mice treated with the high dose of LL-341070 successfully gained as many new cells as they lost even at high levels of loss (Fig. 4B), restoring oligodendrocyte numbers to pre-injury population across all loss levels (Fig. 4C, D) and eliminating the relationship between oligodendrocyte loss and the number of oligodendrocytes at seven weeks (Fig. 4D). Thus, endogenous remyelination fails to restore oligodendrocyte numbers in mice with high levels of oligodendrocyte loss, while thyromimetic treatment specifically ameliorates this deficit without altering the regenerative response to low levels of oligodendrocyte loss.

### Thyromimetic restores oligodendrocyte numbers to pre-cuprizone levels and largely restores myelin content to healthy levels

Over the experimental period of demyelination and remyelination, healthy mice continue to generate new oligodendrocytes<sup>14,41</sup>. Thus, we sought not only to determine the ability of LL-341070 to restore the original number of oligodendrocytes (baseline), but to generate the number of oligodendrocytes that would be expected if the mice never incurred a demyelinating injury (healthy). We imaged and tracked V1 oligodendrogenesis in age-matched healthy mice over the same period (10.5 weeks total). Healthy mice had  $122 \pm 2$  (mean  $\pm$  SEM) % of their baseline oligodendrocytes by three weeks post-cuprizone and  $135 \pm 6$  % by seven weeks (Fig. 4E and Supplementary Fig. 10A–B). Remyelinating mice treated with low or high dose LL-341070 restored baseline oligodendrocyte numbers by seven weeks (Fig. 4E and Supplementary Fig. 10B), but no remyelinating group – regardless of drug treatment – restored oligodendrocytes to healthy levels at either timepoint (Fig. 4E and Supplementary Fig. 10A, B). We expect that the regenerative oligodendrogenesis response had ended by seven weeks, given that oligodendrocyte gain during remyelination is driven by loss one week prior (Fig. 2F, G) and oligodendrocyte loss ceased by approximately three weeks (Fig. 1E and Supplementary Fig. 4A, D). Indeed, by seven weeks, the oligodendrogenesis rate of remyelinating mice was no longer higher than that of healthy mice (Fig. 4F and Supplementary Fig. 8F–I), indicating that the regenerative oligodendrogenesis response had largely concluded by this timepoint and remyelinating mice will not readily reach healthy levels of oligodendrocytes. Modeling of future oligodendrocyte levels in remyelinating and healthy mice supports this idea (Supplementary Table 2).

Previous studies have found that remyelinating oligodendrocytes make longer sheaths<sup>42,44</sup> or temporarily more sheaths<sup>21</sup> than new oligodendrocytes in healthy mice. Thus, myelin may recover to healthy levels while oligodendrocyte numbers do not. To investigate this possibility, we traced the sheaths made by a subset of new EGFP+ oligodendrocytes in healthy and remyelinating mice (Fig. 4G, H). We found no differences between healthy and remyelinating mice in sheath number (Fig. 4I), average sheath length (Supplementary Fig. 10C), or total myelin length (Supplementary Fig. 10D) per new oligodendrocyte, although there was a trend of increased sheath number in the remyelinating groups compared to healthy mice. Additionally, there were no differences between vehicle-treated or thyromimetic-treated mice in any parameters (Fig. 4I and Supplementary Fig. 10C, D), indicating that LL-341070 does not alter the amount of myelin made by new oligodendrocytes. Next, using the values for each group of sheath number and total sheath length per new oligodendrocyte, we estimated the total number of sheaths (Fig. 4J and Supplementary Fig. 10F, G) or sheath length (Supplementary Fig. 10E, H, I) per mouse at three and seven weeks post-cuprizone (see *Statistics and modeling* in Methods). We find that thyromimetic-treated mice restored their baseline levels of myelin by three weeks (Fig. 4J and Supplementary Fig. 10E, F, H), and largely returned to



healthy levels of myelin by seven weeks (Fig. 4J and Supplementary Fig. 10E, G, I), while vehicle-treated mice remained well below healthy levels of myelin (Fig. 4J and Supplementary Fig. 10E-I). Thus, by temporarily increasing oligodendrogenesis in mice with severe demyelination, thymimetic treatment restores baseline oligodendrocyte numbers by seven weeks, largely restoring myelin content to healthy levels.

### Regenerative oligodendrogenesis is enhanced more quickly and robustly by LL-341070 compared to clemastine

Previous work shows that clemastine enhances remyelination in mouse models of demyelination and shows benefits in multiple sclerosis patients<sup>4,27,37,58</sup>. We sought to compare the efficacy of LL-341070 in promoting oligodendrocyte gain during remyelination to clemastine. In parallel cohorts, mice were treated with clemastine

**Fig. 3 | Thyromimetic treatment enhances oligodendrocyte gain during remyelination.** **A** Hydrolysis of LL-341070 into its active form by CNS-enriched fatty acid amide hydrolase (FAAH). **B** Experimental timeline. **C** Treatment groups. **D** Cumulative OL loss and gain (as a percentage of baseline OLs) in individual mice over time (vehicle:  $n = 7$ , 0.1 mg/kg;  $n = 7$ , 0.3 mg/kg;  $n = 6$ ). **E** Cumulative OL loss by 3 weeks does not differ between groups in mean or variance. **F** Representative images of V1 OLs at 1.5 weeks post-cuprizone. Locations of lost OLs (dark blue) and new OLs (light blue) are circled. Additional timepoints in Supplementary Fig. 7. **G** ANCOVA with unequal slopes shows effect of treatment, cumulative OL loss, and interaction between cumulative OL loss and treatment on cumulative OL gain at 1.5 weeks. **H** High dose LL-341070 increases cumulative OL gain at 1.5 weeks. Low dose LL-341070 increases cumulative OL gain after 7 weeks. **I** High dose LL-341070 increases maximum OL gain rate (as a percentage of baseline OLs/day) during remyelination. **J** High dose LL-341070 increases OL gain rate (as a percentage of baseline OLs/day) only between 0 and 1.5 weeks. In **(E)**, ANOVA ( $F(2, 14) = 0.29$ ,  $p = 0.75$ ). Brown-Forsythe ( $F(2, 14) = 1.05$ ,  $p = 0.37$ ). Vehicle:  $n = 7$ ; 0.1 mg/kg:  $n = 7$ ; 0.3 mg/kg:  $n = 6$ . In **(G)**, ANCOVA with unequal slopes ( $F(5, 18) = 9.5$ ,  $***p = 0.0001$ ).

Effects: treatment ( $F = 7.91$ ,  $**p = 0.0034$ ), OL loss ( $F = 23.33$ ,  $***p = 0.0001$ ), interaction ( $F = 6.41$ ,  $**p = 0.0079$ ). Vehicle:  $n = 8$ , 0.1 mg/kg:  $n = 9$ , 0.3 mg/kg:  $n = 7$ . In **(H)** 1.5w, Tukey's HSD (0.3 mg/kg vs. vehicle:  $**p = 0.0025$ ; 0.3 mg/kg vs. 0.1 mg/kg:  $*p = 0.049$ ). Vehicle:  $n = 8$ , 0.1 mg/kg:  $n = 9$ , 0.3 mg/kg:  $n = 7$ . In **(H)** 3w, Tukey's HSD (0.3 mg/kg vs. vehicle:  $p = 0.055$ ). Vehicle:  $n = 7$ , 0.1 mg/kg:  $n = 7$ , 0.3 mg/kg:  $n = 6$ . In **(H)** 7w, Tukey's HSD (0.3 mg/kg vs. vehicle,  $p = 0.051$ ; 0.1 mg/kg vs. vehicle,  $*p = 0.034$ ). Vehicle:  $n = 5$ , 0.1 mg/kg:  $n = 4$ , 0.3 mg/kg:  $n = 5$ . In **(I)**, Tukey's HSD (0.3 mg/kg vs. vehicle:  $*p = 0.018$ ). Vehicle:  $n = 7$ , 0.1 mg/kg:  $n = 7$ , 0.3 mg/kg:  $n = 6$ . In **(J)** 0-1.5w, Tukey's HSD (0.3 mg/kg vs. vehicle:  $**p = 0.0012$ ; 0.3 mg/kg vs. 0.1 mg/kg:  $*p = 0.025$ ). Vehicle:  $n = 8$ , 0.1 mg/kg:  $n = 9$ , 0.3 mg/kg:  $n = 7$ . In **(J)** 1.5-3w, ANCOVA with unequal slopes in Supplementary Fig. 8G not significant. Vehicle:  $n = 7$ ; 0.1 mg/kg:  $n = 7$ ; 0.3 mg/kg:  $n = 6$ . In **(J)** 3-5w, ANCOVA with unequal slopes in Supplementary Fig. 8H not significant. Vehicle:  $n = 6$ , 0.1 mg/kg:  $n = 4$ , 0.3 mg/kg:  $n = 5$ .  $*p < 0.05$ ,  $**p < 0.01$ ; least square mean  $\pm$  SEM in **(H-J)**;  $n$ =mice; two-sided statistical tests. See Supplementary Data 1 for statistical details and Source Data file for source data. OL=oligodendrocyte, VI=primary visual cortex.

(10 mg/kg) or vehicle (10% DMSO) for the first three weeks of remyelination and underwent longitudinal in vivo two-photon imaging of V1 to track oligodendrocyte loss and gain over time (Fig. 5A, B).

First, we assessed oligodendrocyte loss between groups. Mice treated with vehicle or clemastine exhibited a wide range in loss, with no differences in mean or variance between groups (Fig. 5C). Next, we examined oligodendrocyte gain during remyelination and found differences in the timing of efficacy of LL-341070 and clemastine. While high dose LL-341070 treatment robustly increased oligodendrocyte gain rate during the first half of treatment (Fig. 3J), the strongest effects of clemastine on oligodendrocyte gain rate occurred after treatment ended (Fig. 5D and Supplementary Fig. 11A–C). A difference in the magnitude of the effects of LL-341070 and clemastine was also apparent. While 0.3 mg/mL LL-341070 doubled the maximum oligodendrocyte gain rate (Fig. 3I), the tested dose of clemastine did not significantly impact this metric (Fig. 5E and Supplementary Fig. 11D–F). These dynamics resulted in no statistically detectable differences in cumulative new oligodendrocytes in mice treated with clemastine compared to vehicle-treated mice (Fig. 5F and Supplementary Fig. 11G–I).

Finally, we assessed whether clemastine – like LL-341070 – was able to ameliorate the regeneration deficit at high oligodendrocyte loss levels. We found that this was not the case; rather, a correlation persisted between oligodendrocyte loss and oligodendrocyte number at seven weeks in mice treated with clemastine (Fig. 5G and Supplementary Fig. 11J), indicating that clemastine was unable to fully eliminate the regeneration deficit experienced by mice with high levels of oligodendrocyte loss. Overall, while clemastine enhances oligodendrocyte gain rate, the tested dose of LL-341070 is more effective at augmenting oligodendrocyte gain rate, cumulative oligodendrocyte gain, and restoration of oligodendrocyte numbers after severe demyelination.

### The recovery of single-neuron latency is accelerated by LL-341070

Given the robust effects of LL-341070 in promoting remyelination, we sought to test whether this treatment could enhance the restoration of neuronal function in the primary visual cortex following demyelination. Demyelination delays visual-induced population responses in the visual cortex known as visual evoked potentials (VEPs), while remyelination rescues VEP latency deficits<sup>27,36,59</sup>. Thus, VEP latency measurements are often used as supportive evidence to help confirm a clinical diagnosis of multiple sclerosis as well as a biomarker for functional improvement in clinical trials<sup>37,60</sup>. However, how demyelination and remyelination affect the visual responses of individual neurons in vivo has remained unexplored. To this end, we used Neuropixels, high-density extracellular recording probes that

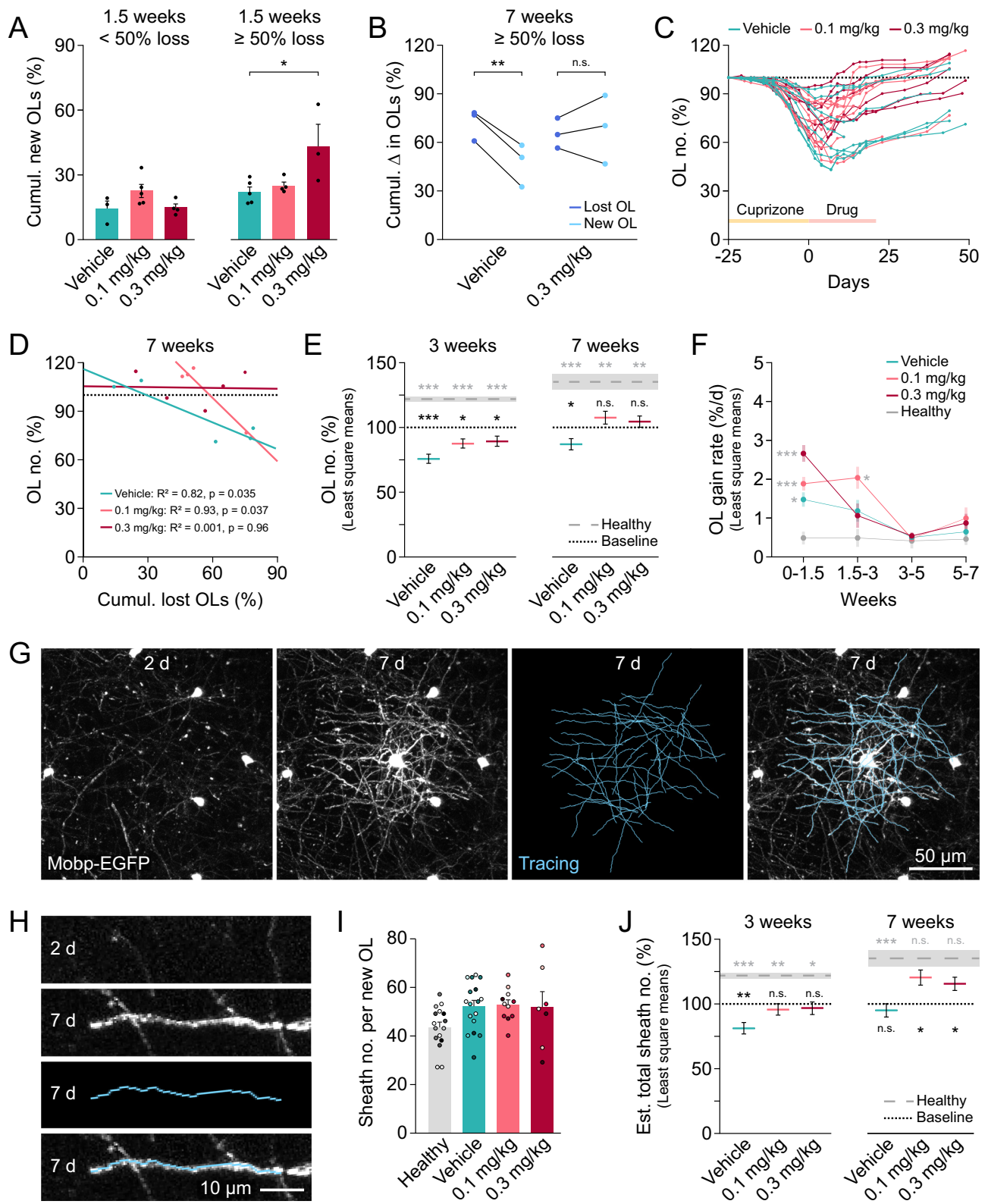
allow for the simultaneous evaluation of VEPs and hundreds of single neurons, implanted into V1 (Fig. 6A). To capture different aspects of visual processing, animals were presented with brief (50 ms), full visual-field luminance changes from mean towards both dark and bright (Supplementary Fig. 12A, B) during the electrophysiological recording. We probed the timing of visually-evoked neural activity in healthy mice, demyelinated mice (end of cuprizone), and mice treated with thyromimetic or vehicle at the end of treatment (three weeks post-cuprizone) or four weeks after the end of the treatment (seven weeks post-cuprizone) (Fig. 6B).

Taking advantage of the multiple recording channels in the Neuropixels probes, we isolated single neurons and analyzed how their response latencies were altered by demyelination and remyelination therapy (Fig. 6C and Supplementary Fig. 12D). Single-neuron responses were delayed after demyelination (Fig. 6D). Three-week treatment with high dose LL-341070 restored the latency to the flashed stimulus, while low dose- and vehicle-treated mice maintained delayed responses (Fig. 6E). When assessing luminance changes to dark or bright individually, we found that responses to both stimuli were delayed by cuprizone (Supplementary Fig. 13A, D) and rescued by high dose LL-341070 for 3 weeks (Supplementary Fig. 13B, E). Meanwhile, at this timepoint, responses to dark remained delayed in vehicle-treated mice, while responses to bright were still slowed in mice treated with low dose LL-341070 (Supplementary Fig. 13B, E). Overall, these data support an effect of thyromimetic treatment in accelerating the recovery of single-neuron response latencies after demyelination.

### Restoration of visual evoked potentials is accelerated by LL-341070

VEPs capture the summed input and neuronal network response to a visual stimulus in cortex, which may reflect the underlying deficits in neuronal activity and connectivity in V1. Therefore, we measured VEPs from local field potentials (LFPs) recorded by the Neuropixels probes (Fig. 6F and Supplementary Fig. 12C). We first assessed the timing and amplitude of the VEP. We found no significant differences between groups in latency of the first negative peak (N70), which is thought to correlate to the arrival of the thalamic input in V1 (Fig. 6G, H, and Supplementary Fig. 14A, B, D, E). Similarly, we only detected small changes in amplitude of the first positive peak (P100) in relation to N70 (Supplementary Fig. 15A, B, D, E, G, H). However, we observed that VEP structure appeared less organized in demyelinated mice compared to healthy controls (Fig. 6F). To quantify these differences, we developed a shape distortion metric, which quantifies the distance between a given trial VEP and the average VEP of healthy mice (see *In vivo electrophysiology: spike sorting and pre-processing* in Methods). Using this metric, we found that demyelinated mice exhibited altered VEP shape





as compared to healthy controls (Fig. 6I and Supplementary Fig. 14G, J). Importantly, the demyelination-triggered distortion in VEP shape was rescued by three weeks post-cuprizone in mice treated with the high dose of LL-341070, while low dose- and vehicle-treated mice maintained an altered VEP shape (Fig. 6J). Therefore, in concert with accelerating oligodendrocyte regeneration, thymimetic treatment enhances the recovery of V1 single neuron and population responses to visual stimuli.

### Partial remyelination can recover visual responses

Since visual responses were still impaired in vehicle- and low dose-treated mice after three weeks of remyelination, when remyelination was still ongoing, we assessed visual responses four weeks later, after seven weeks of remyelination. Between three and seven weeks post-cuprizone, single neuron responses improved in mice treated with vehicle or low dose LL-341070, while neuronal responses of mice treated with high dose LL-341070 did not change (Fig. 7A). Thus, mice

**Fig. 4 | Thyromimetic LL-341070 enhances oligodendrocyte gain to a greater extent after moderate or severe demyelination to restore oligodendrocytes and myelin.** **A** High dose LL-341070 increases cumulative OL gain only in mice with  $\geq 50\%$  cumulative OL loss (as a percentage of baseline OLs). **B** High dose LL-341070 rescues regeneration deficit after severe demyelination. **C** OL number (as a percentage of baseline OLs) in individual mice over time (vehicle:  $n = 7$ , 0.1 mg/kg:  $n = 7$ , 0.3 mg/kg:  $n = 6$ ). Dashed line at 100%. **D** High dose LL-341070 eliminates correlation between OL number and cumulative OL loss at 7 weeks. Dashed line at 100%. **E** Low and high dose LL-341070 recover baseline but not healthy OL levels by 7 weeks. Vehicle does not recover baseline OL levels. **F** Oligodendrogenesis rate of remyelinating mice returns to that of healthy mice after 3 weeks. **G** Representative image of a new OL analyzed 7 days post-cuprizone and its traced sheaths (blue). **H** High magnification image of a single traced sheath (blue) from cell in **(G)**. **I** No difference between groups in number of sheaths made by individual new oligodendrocytes. **J** LL-341070 recovers baseline myelin levels by 3 weeks of remyelination and achieves roughly healthy myelin levels by 7 weeks. See Methods for myelin level estimation protocol. In **(A)**  $< 50\%$  loss, ANOVA ( $F(2, 9) = 2.80, p = 0.11$ ). Vehicle:  $n = 3$ , 0.1 mg/kg:  $n = 5$ , 0.3 mg/kg:  $n = 4$ . In **(A)**  $\geq 50\%$  loss, ANOVA ( $F(2, 9) = 5.09, *p = 0.033$ ). Tukey's HSD (0.3 mg/kg vs. vehicle:  $*p = 0.032$ ). Vehicle:  $n = 5$ , 0.1 mg/kg:  $n = 4$ , 0.3 mg/kg:  $n = 3$ . In **(B)** vehicle, paired t test ( $t(2) = 10.12, **p = 0.0096, n = 3$ ). In **(B)** 0.3 mg/kg, paired t test ( $t(2) = 0.47, p = 0.69, n = 3$ ). In **(D)** vehicle, linear regression ( $F(1, 3) = 13.4, n = 5$ ). In **(D)** 0.1 mg/kg, linear regression ( $F(1, 2) = 25.53, n = 4$ ). In **(D)** 0.3 mg/kg, linear regression ( $F(1, 3) = 0.0033, n = 5$ ). In **(E)** 3w, ANOVA to compare to healthy ( $F(3, 19) = 18.33, ***p < 0.0001$ ). Dunnett's (vehicle vs. healthy:  $***p = 0.0001$ ; 0.1 mg/kg vs. healthy:  $***p = 0.0001$ ; 0.3 mg/kg vs. healthy:  $***p = 0.0002$ ). One-sample t tests to compare to baseline (vehicle vs. baseline:  $t(6) = 6.87, ***p = 0.0005$ ; 0.1 mg/kg vs. baseline:  $t(6) = 3.55, *p = 0.012$ ; 0.3 mg/kg vs. baseline:  $t(5) = 2.75, *p = 0.04$ ). Vehicle:  $n = 7$ , 0.1 mg/kg:  $n = 7$ , 0.3 mg/kg:  $n = 6$ , healthy:  $n = 3$ . In **(E)** 7w, ANOVA to compare to healthy ( $F(3, 13) = 14.96, ***p = 0.0002$ ). Dunnett's (vehicle vs. healthy:  $***p < 0.0001$ ; 0.1 mg/kg vs. healthy:

$**p = 0.0073$ ; 0.3 mg/kg vs. healthy:  $**p = 0.0025$ ). One-sample t tests to compare to baseline (vehicle vs. baseline:  $t(4) = 2.99, *p = 0.04$ ; 0.1 mg/kg vs. baseline:  $t(3) = 1.52, p = 0.22$ ; 0.3 mg/kg vs. baseline:  $t(4) = 1.04, p = 0.36$ ). Vehicle:  $n = 5$ , 0.1 mg/kg:  $n = 4$ , 0.3 mg/kg:  $n = 5$ , healthy:  $n = 3$ . In **(F)** 0-1.5w, ANOVA ( $F(3, 24) = 16.81, ***p < 0.0001$ ). Dunnett's (vehicle vs. healthy:  $*p = 0.011$ ; 0.1 mg/kg vs. healthy:  $***p = 0.0004$ ; 0.3 mg/kg vs. healthy:  $***p = 0.0001$ ). Vehicle:  $n = 8$ , 0.1 mg/kg:  $n = 9$ , 0.3 mg/kg:  $n = 7$ , healthy:  $n = 4$ . In **(F)** 1.5-3w, ANOVA ( $F(3, 19) = 3.95, *p = 0.024$ ). Dunnett's (vehicle vs. healthy:  $p = 0.39$ ; 0.1 mg/kg vs. healthy:  $*p = 0.016$ ; 0.3 mg/kg vs. healthy:  $p = 0.55$ ). Vehicle:  $n = 7$ , 0.1 mg/kg:  $n = 7$ , 0.3 mg/kg:  $n = 6$ , healthy:  $n = 3$ . In **(F)** 3-5w, ANOVA ( $F(3, 14) = 0.21, p = 0.89$ ). Vehicle:  $n = 6$ , 0.1 mg/kg:  $n = 4$ , 0.3 mg/kg:  $n = 5$ , healthy:  $n = 3$ . In **(F)** 5-7w, ANOVA ( $F(3, 13) = 0.78, p = 0.52$ ). Vehicle:  $n = 5$ , 0.1 mg/kg:  $n = 4$ , 0.3 mg/kg:  $n = 5$ , healthy:  $n = 3$ . In **(I)**, ANOVA ( $F(3,47) = 2.72, p = 0.055$ ). Vehicle:  $n = 17$  OLs from 7 mice, 0.1 mg/kg:  $n = 11$  OLs from 6 mice, 0.3 mg/kg:  $n = 7$  OLs from 5 mice, healthy:  $n = 16$  OLs from 7 mice. Data points color-coded by mouse. In **(J)** 3w, ANOVA to compare to healthy ( $F(3, 19) = 10.06, ***p = 0.0003$ ). Dunnett's (vehicle vs. healthy:  $***p = 0.0001$ ; 0.1 mg/kg vs. healthy:  $**p = 0.0070$ ; 0.3 mg/kg vs. healthy:  $*p = 0.012$ ). One-sample t tests to compare to baseline (vehicle vs. baseline:  $t(6) = 4.45, **p = 0.0043$ ; 0.1 mg/kg vs. baseline:  $t(6) = 1, p = 0.35$ ; 0.3 mg/kg vs. baseline:  $t(5) = 0.63, p = 0.55$ ). Vehicle:  $n = 7$ , 0.1 mg/kg:  $n = 7$ , 0.3 mg/kg:  $n = 6$ , healthy:  $n = 3$ . In **(J)** 7w, ANOVA to compare to healthy ( $F(3, 13) = 8.37, **p = 0.0023$ ). Dunnett's (vehicle vs. healthy:  $**p = 0.0010$ ; 0.1 mg/kg vs. healthy:  $p = 0.27$ ; 0.3 mg/kg vs. healthy:  $p = 0.090$ ). One-sample t tests to compare to baseline (vehicle vs. baseline:  $t(4) = 0.96, p = 0.39$ ; 0.1 mg/kg vs. baseline:  $t(3) = 3.45, *p = 0.041$ ; 0.3 mg/kg vs. baseline:  $t(4) = 2.98, *p = 0.041$ ). Vehicle:  $n = 5$ , 0.1 mg/kg:  $n = 4$ , 0.3 mg/kg:  $n = 5$ , healthy:  $n = 3$ . n.s. not significant,  $*p < 0.05, **p < 0.01, ***p < 0.001$ ; mean  $\pm$  SEM in **(A, I)**; treatments: least square mean  $\pm$  SEM and healthy: mean  $\pm$  SEM in **(E, F, J)**; lines of best fit in **(D)**;  $n$ =mice unless otherwise specified; two-sided statistical tests. See Supplementary Data 1 for statistical details and Source Data file for source data. OL=oligodendrocyte.

treated with high dose LL-341070 reached a plateau of recovery by three weeks while the other groups continued to improve. By seven weeks, we found no differences between the treatment groups in any of the evaluated parameters and most responses were similar in range to those of healthy mice (Fig. 7B, C, Supplementary Fig. 13C, F, Supplementary Fig. 14C, F, I, L, and Supplementary Fig. 15C, F, I). However, single neuron latency of the vehicle group remained delayed compared to healthy mice (Fig. 7B). Additionally, the shape distortion of VEP responses at seven weeks of all groups was different from healthy mice (Fig. 7D). This difference may be due to age-related VEP changes (healthy responses were measured 10.5 weeks earlier), ongoing compensatory effects on V1 neural responses over the course of remyelination, or incomplete restoration to healthy conditions.

Given that thyromimetic treatment accelerated the restoration of both oligodendrocyte numbers and neuronal function, we sought to investigate the level of cortical remyelination necessary to recover neuronal function. Single neuron latency was recovered in high dose LL-341070 at three weeks (Fig. 6E) with  $89 \pm 4$  (least square means  $\pm$  SEM) % of baseline oligodendrocytes (Figs. 4E and 7E) and an estimated  $97 \pm 5$  % of baseline myelin (Figs. 4J and 7E), with oligodendrocytes below baseline and healthy levels and myelin below healthy levels. Thus, full recovery of cortical oligodendrocytes or myelin to healthy levels is not required to restore deficits in visual neuronal responses. In contrast, we did not observe recovered single neuron latency in low dose LL-341070 at three weeks ( $87 \pm 4$  % of baseline oligodendrocytes and  $96 \pm 4$  % of baseline myelin) or vehicle at seven weeks ( $87 \pm 4$  % of baseline oligodendrocytes and  $95 \pm 5$  % of baseline myelin) (Figs. 4E, J, 6E, and 7B, E). Thus, recovery of oligodendrocytes and myelin to a similar level does not necessarily restore visual function. Low dose LL-341070 recovered single neuron latency (Fig. 7B, E) at seven weeks post-cuprizone ( $108 \pm 5$  % of baseline oligodendrocytes and  $120 \pm 6$  % of baseline myelin, statistically recovering oligodendrocytes to baseline levels and myelin to healthy levels (Figs. 4E, J, 7E)). Together these results indicate that the relationship between remyelination levels and restoration of visual responses is complex and does not solely depend

on the total level of remyelination. However, functional recovery can be achieved with incomplete remyelination.

## Discussion

Myelin loss, including in visual gray matter, is a common feature of several neurodegenerative diseases and injury conditions, and is present in normal aging<sup>8-14</sup>. In addition, myelin is malformed or present in insufficient levels in several neurodevelopmental and neuropsychiatric disorders<sup>61-66</sup>. By promoting formation of new oligodendrocytes and myelin, remyelination therapies may be clinically important for numerous neurological conditions. However, progress may be hampered by our incomplete understanding of the remyelination process and lack of clinically available remyelination therapies.

In this study, we used in vivo microscopy and neurophysiology approaches to unravel important aspects of remyelination in the visual system. We found that oligodendrocyte gain during remyelination is driven by recent oligodendrocyte loss and demonstrated that oligodendrocyte regeneration fails when high rates of demyelination occur quickly. Advancing our understanding of therapeutic-induced remyelination, we found that distinct drugs stimulate oligodendrocyte gain with different temporal dynamics and that remyelination therapy is loss-dependent and only effective when demyelination is moderate or severe. Importantly, we demonstrated that the new thyromimetic LL-341070 is a highly potent remyelination therapeutic, which accelerates oligodendrocyte regeneration and recovery of neuronal function. Moreover, our data showed that even partial remyelination can restore metrics of visual neuronal function. While remyelination to healthy levels is not required to restore visual neuronal responses, there is no clearly defined threshold of regeneration that restores function, and other features of remyelination, such as timing and pattern of remyelination, likely contribute to functional recovery.

While remyelination is widely observed following a demyelinating injury<sup>21,24,44,45</sup>, the cellular and molecular triggers of this response are unknown. We found that oligodendrocyte gain rate during remyelination is driven by recent oligodendrocyte loss rather than a drive to

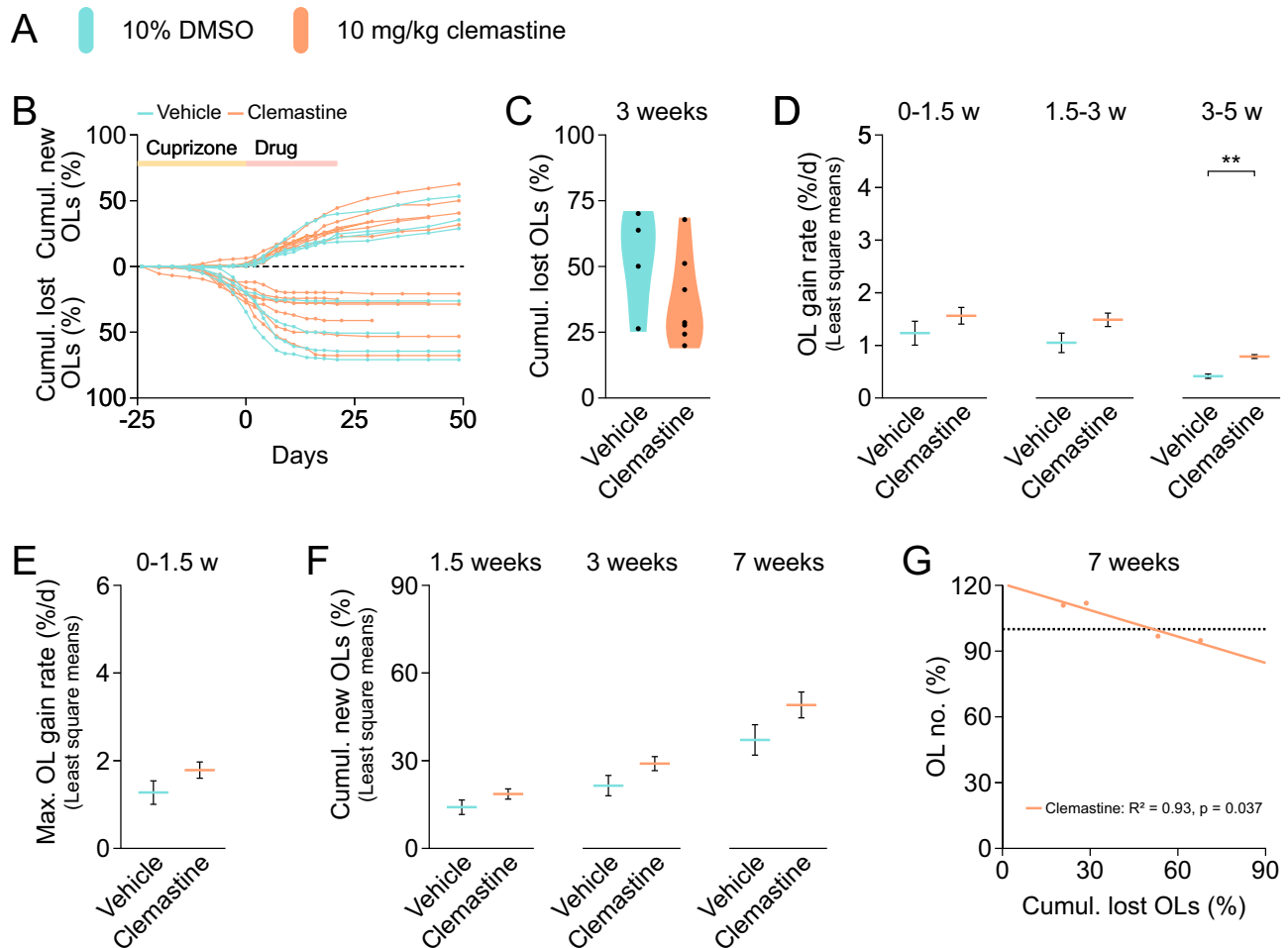


**Fig. 5 | Clemastine has subtler and more protracted actions on remyelination.**

**A** Treatment groups. **B** Cumulative OL loss and gain (as a percentage of baseline OLs) in individual mice over time (vehicle:  $n = 4$ , clemastine:  $n = 7$ ). **C** Cumulative OL loss at 3 weeks does not differ between groups in mean or variance. **D** Clemastine increases OL gain rate (as a percentage of baseline OLs/day) from 3 to 5 weeks. **E** Clemastine does not change maximum OL gain rate (as a percentage of baseline OLs/day) during remyelination. **F** Clemastine does not significantly increase cumulative OL gain. **G** OL number (as a percentage of baseline OLs) is correlated with cumulative OL loss at 7 weeks in mice treated with clemastine. In **(C)**,  $t$  test ( $t(9) = -1.37$ ,  $p = 0.20$ ). Brown-Forsythe ( $F(1,9) = 0.043$ ,  $p = 0.84$ ). Vehicle:  $n = 4$ , clemastine:  $n = 7$ . In **(D)** 0-1.5w, ANCOVA with unequal slopes in Supplementary

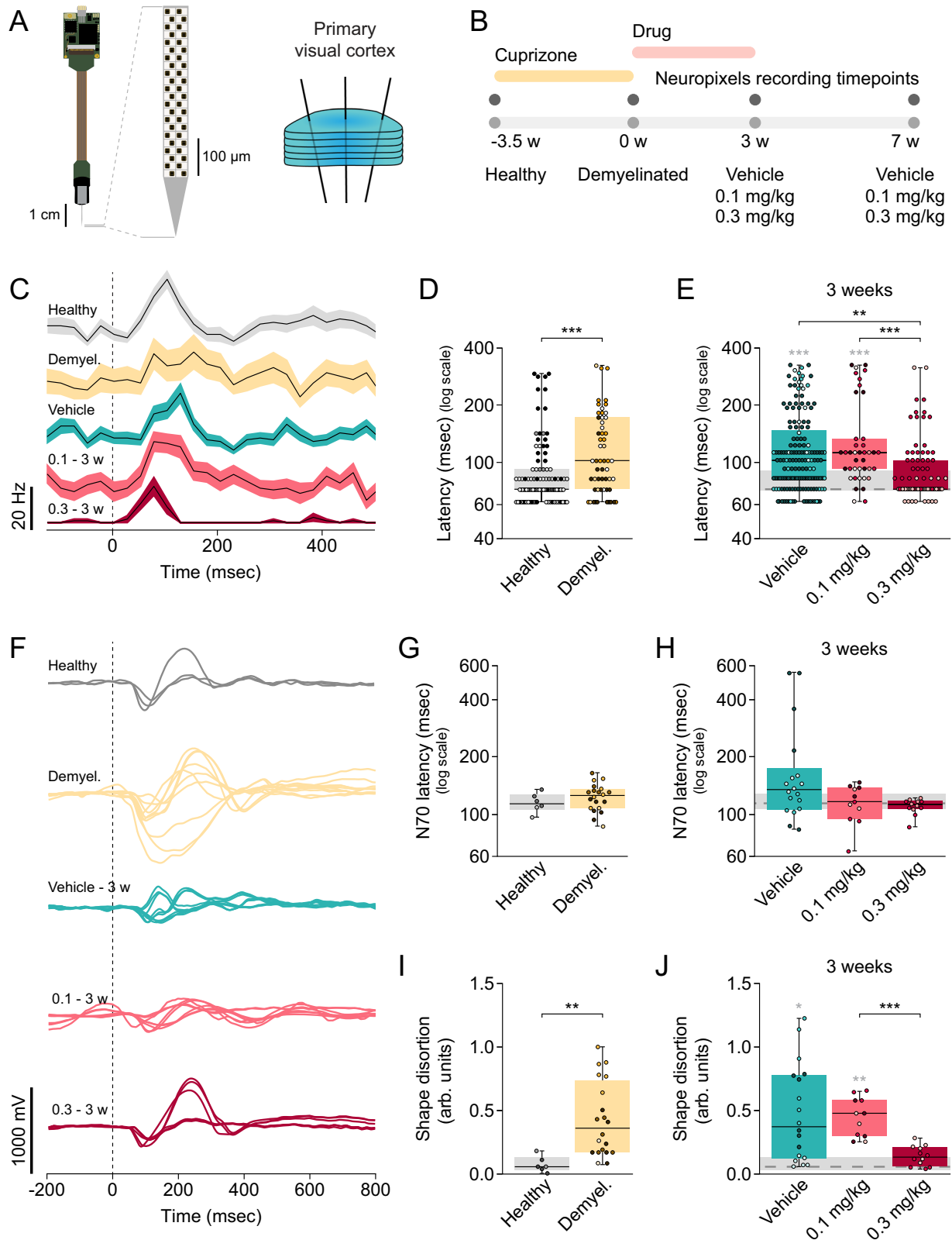
Fig. 11A not significant. Vehicle:  $n = 4$ , clemastine:  $n = 7$ . In **(D)** 1.5-3w, no effect of treatment in ANCOVA with unequal slopes in Supplementary Fig. 11B. Vehicle:  $n = 4$ , clemastine:  $n = 7$ . In **(D)** 3-5w, post-hoc  $t$  test ( $t(5) = 6.73$ ,  $**p = 0.0011$ ). Vehicle:  $n = 4$ , clemastine:  $n = 5$ . In **(E)**, ANCOVA with unequal slopes in Supplementary Fig. 11F not significant. Vehicle:  $n = 4$ , clemastine:  $n = 7$ . In **(F)**, ANCOVA with unequal slopes in Supplementary Fig. 11G-I not significant. 1.5 and 3w: vehicle:  $n = 4$ , clemastine:  $n = 7$ . 7w: vehicle:  $n = 3$ , clemastine:  $n = 7$ . In **(G)**, linear regression ( $F(1, 2) = 25.75$ ,  $n = 4$ ).  $**p < 0.01$ ; mean  $\pm$  SEM in **(C)**; least square mean  $\pm$  SEM in **(D-F)**; line of best fit in **(G)**;  $n =$  mice; two-sided statistical tests. See Supplementary Data 1 for statistical details and Source Data file for source data. OL=oligodendrocyte.

reestablish oligodendrocyte numbers (Fig. 2E-G), indicating that acute signaling around the time of the loss of myelinating oligodendrocytes induces new oligodendrocyte formation. However, the exact source of the signal is unknown, and it is unclear if it involves direct signaling from damaged oligodendrocytes or is mediated by other cell types. Previous work found that new oligodendrocyte generation temporally correlates better with myelin loss and microglial activation than with the laser ablation of oligodendrocyte cell bodies<sup>44</sup>. Together with these findings, our work suggests that the pro-remyelinating signal(s) may derive, among other options, from microglial activation or phagocytosis, oligodendrocyte/myelin degradation or debris, or acute signaling from recently demyelinated axons. Identification of the molecular triggers of remyelination could have important clinical implications, as it may further illuminate causes of remyelination failure and provide additional targets to enhance remyelination.

Despite the occurrence of endogenous remyelination, it is often insufficient, leading to chronic demyelination<sup>26</sup>. We have described two factors that may contribute to this phenomenon. First, we found

evidence of a critical time window for endogenous remyelination shortly following the loss of oligodendrocytes (Fig. 2E-G). For endogenous remyelination to be maximally efficacious, it is essential that new oligodendrocytes can form and survive in this period. Prolonged inhibition of regenerative oligodendrogenesis extending beyond the end of oligodendrocyte loss may occur during demyelinating disease, precluding any endogenous remyelination response. This may contribute to the lack of active remyelination observed in chronic multiple sclerosis lesions despite the presence of OPCs<sup>67</sup>. The inhibitory signal(s) preventing remyelination can be inflammatory, like CCL19<sup>68</sup>, TNF $\alpha$ <sup>69</sup> and IFN- $\beta$ <sup>70</sup>, or non-inflammatory, including accumulation of extracellular matrix molecules, myelin debris, and Nogo receptor 1 signaling<sup>28,71,72</sup>.

Second, we observed deficits in endogenous remyelination in response to high rates of oligodendrocyte loss (Fig. 2H). Mice with moderate or severe demyelination failed to restore their initial oligodendrocyte populations (Fig. 1H) due to extended periods where oligodendrocyte loss exceeded 1.5% per day (Supplementary Fig. 4D). At



these loss rates, endogenous gain rates could not keep up and never exceeded 2.5% per day, despite substantially higher loss rates (Fig. 2H). Endogenous oligodendrocyte gain rates may be limited to this level by intrinsic constraints on the oligodendrogenesis process and/or by extrinsic factors that inhibit this process specifically during high rates of oligodendrocyte loss, such as accumulation of inflammatory mediators, extracellular matrix molecules, or myelin debris, damage to

axons, or reactive gliosis. Enhancing OPC differentiation using LL-341070 induced oligodendrocyte gain rates greatly exceeding 2.5% per day (Fig. 3I, J, and Supplementary Fig. 8E, F) and restored oligodendrocyte numbers even following severe demyelination (Fig. 4C–E). Thus, regardless of how regenerative oligodendrogenesis rates are limited, these data support the longstanding idea that there is untapped differentiation potential of OPCs in endogenous remyelination<sup>73</sup>.

**Fig. 6 | LL-341070 treatment accelerates recovery of visual function after demyelination.** **A** As a terminal procedure, three Neuropixel probes inserted in V1 record neuronal activity during visual stimuli presentation. **B** Experimental timeline. **C** Representative traces (with SEM) of single-neuron responses to dark flash. Dashed line at stimulus onset. **D** Demyelination delays single neuron responses to flash (dark and bright). **E** High dose LL-341070 restores single neuron latencies to flash (dark and bright) by 3 weeks. **F** Representative VEPs in response to a dark flash. Dashed line at stimulus onset. **G, H** VEP N70 latency to flash (dark and bright) is not significantly altered by demyelination (**G**) or treatment at 3 weeks (**H**). **I** Demyelination distorts VEP shape in response to flash (dark and bright). **J** High dose LL-341070 rescues VEP shape distortion by 3 weeks. In (**D**), Wilcoxon ( $Z = 4.37$ ,  $***p < 0.0001$ ). Healthy:  $n = 104$  responses from 6 probes from 3 mice, demyelinated:  $n = 55$  responses from 7 probes from 5 mice. In (**E**), Kruskal-Wallis ( $F(3) = 43.17$ ,  $***p < 0.0001$ ). Steel-Dwass (vehicle vs. healthy:  $***p < 0.0001$ ; 0.1 mg/kg vs. healthy:  $***p < 0.0001$ ; 0.3 mg/kg vs. 0.1 mg/kg:  $***p = 0.0002$ ; 0.3 mg/kg vs. vehicle  $***p = 0.0022$ ). Vehicle:  $n = 157$  responses from 8 probes from 3 mice, 0.1 mg/kg:  $n = 40$  responses from 6 probes from 4 mice, 0.3 mg/kg:  $n = 76$

responses from 4 probes from 2 mice, healthy:  $n = 104$  responses from 6 probes from 3 mice. In (**G**), Wilcoxon ( $Z = -0.79$ ,  $p = 0.43$ ). Healthy:  $n = 6$  VEPs from 3 probes from 2 mice, demyelinated:  $n = 20$  VEPs from 10 probes from 4 mice. In (**H**), Kruskal-Wallis ( $F(3) = 6.11$ ,  $p = 0.11$ ). Vehicle:  $n = 18$  VEPs from 9 probes from 3 mice, 0.1 mg/kg:  $n = 11$  VEPs from 8 probes from 3 mice, 0.3 mg/kg:  $n = 12$  VEPs from 6 probes from 2 mice, healthy:  $n = 6$  VEPs from 3 probes from 2 mice. In (**I**), Wilcoxon ( $Z = -3.13$ ,  $**p = 0.0017$ ). Healthy:  $n = 6$  VEPs from 3 probes from 2 mice, demyelinated:  $n = 20$  VEPs from 10 probes from 4 mice. In (**J**), Kruskal-Wallis ( $F(3) = 20.38$ ,  $***p = 0.0001$ ). Steel-Dwass (vehicle vs. healthy:  $*p = 0.024$ , 0.1 mg/kg vs. healthy:  $**p = 0.006$ , 0.3 mg/kg vs. 0.1 mg/kg  $***p = 0.0005$ ). Vehicle:  $n = 18$  VEPs from 9 probes from 3 mice, 0.1 mg/kg:  $n = 11$  VEPs from 8 probes from 3 mice, 0.3 mg/kg:  $n = 12$  VEPs from 6 probes from 2 mice, healthy:  $n = 6$  VEPs from 3 probes from 2 mice.  $*p < 0.05$ ,  $**p < 0.01$ ,  $***p < 0.001$ ; median, IQR (box), min./max. (whiskers) in (**D, E, G, H, I, J**); data points color-coded by mouse in (**D, E, G, H, I, J**); two-sided statistical tests. See Supplementary Data 1 for statistical details and Source Data file for source data. VEP=visual evoked potential.

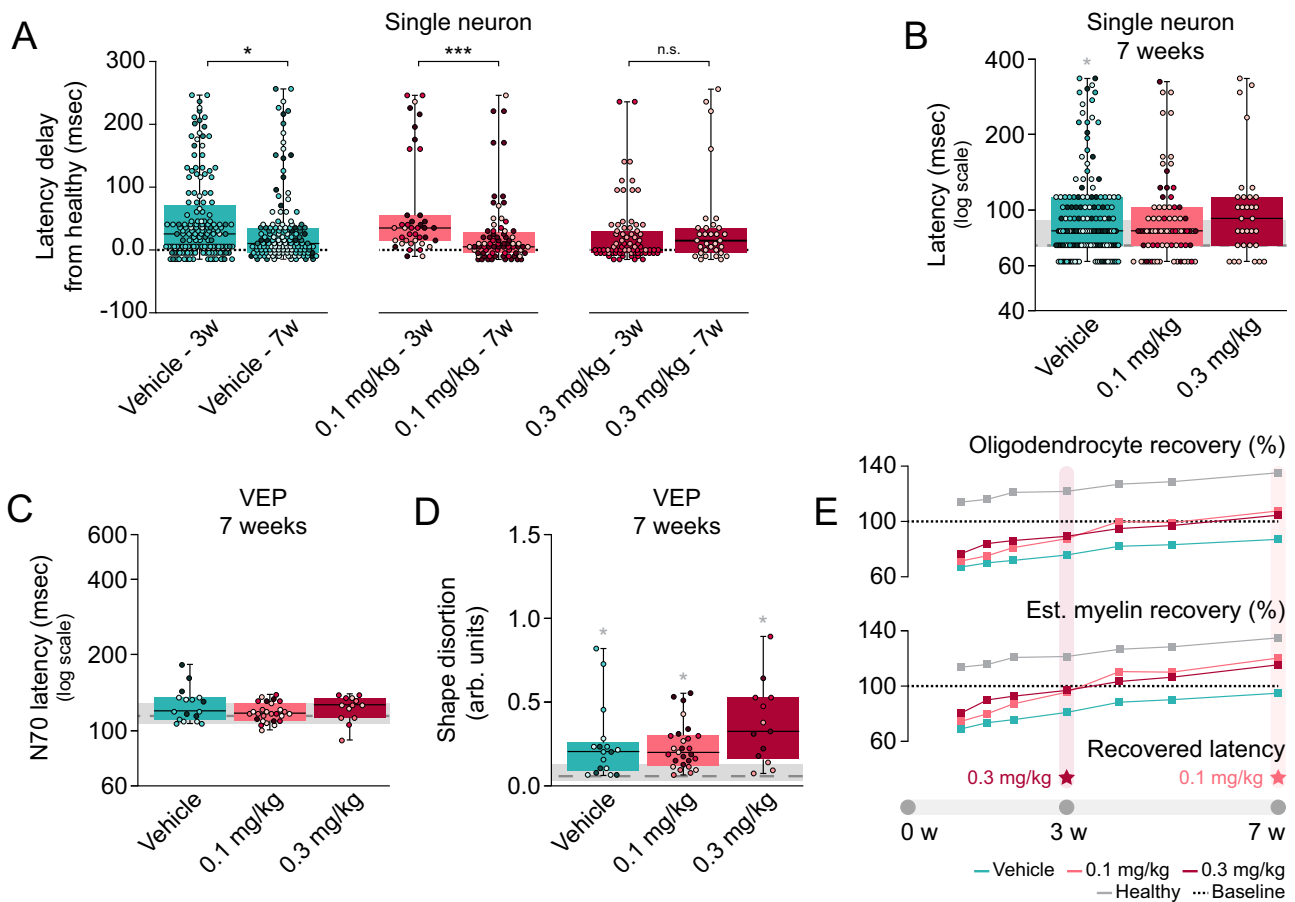


**Fig. 7 | Functional rescue of visual neuronal responses can be attained with remyelination below healthy levels.** **A** Vehicle and low dose LL-341070 improve single-neuron latency to flash (dark and bright) from 3-7 weeks. High dose LL-341070 already recovers by 3 weeks. **B** Low and high dose LL-341070 restore single-neuron latencies to flash (dark and bright) by 7 weeks. **C, D** No differences between groups in VEP N70 latency (**C**) or shape (**D**) to flash (dark and bright) at 7 weeks. **E** Recovery of oligodendrocytes, myelin, and single-neuron responses with time. In (**A**) vehicle, Wilcoxon ( $Z = -2.3$ ,  $*p = 0.022$ ). 3w:  $n = 157$  responses from 8 probes from 3 mice, 7w:  $n = 144$  responses from 11 probes from 4 mice. In (**A**) 0.1 mg/kg, Wilcoxon ( $Z = 4.05$ ,  $***p < 0.0001$ ). 3w:  $n = 40$  responses from 6 probes from 4 mice, 7w:  $n = 77$  responses from 8 probes from 3 mice. In (**A**) 0.3 mg/kg, Wilcoxon ( $Z = 1.11$ ,  $p = 0.27$ ). 3w:  $n = 76$  responses from 4 probes from 2 mice, 7w:  $n = 32$  responses from 3 probes from 1 mouse. In (**B**), Kruskal-Wallis ( $F(3) = 10.85$ ,  $*p = 0.013$ ). Steel-Dwass (vehicle vs. healthy:  $*p = 0.013$ ). Vehicle:  $n = 144$  responses

from 11 probes from 4 mice, 0.1 mg/kg:  $n = 77$  responses from 8 probes from 3 mice, 0.3 mg/kg:  $n = 32$  responses from 3 probes from 1 mouse, healthy:  $n = 104$  responses from 6 probes from 3 mice. In (**C**), Kruskal-Wallis ( $F(3) = 3.32$ ,  $p = 0.34$ ). Vehicle:  $n = 17$  VEPs from 9 probes from 3 mice, 0.1 mg/kg:  $n = 27$  VEPs from 14 probes from 5 mice, 0.3 mg/kg:  $n = 13$  VEPs from 9 probes from 3 mice, healthy:  $n = 6$  VEPs from 3 probes from 2 mice. In (**D**), Kruskal-Wallis ( $F(3) = 13.22$ ,  $p = 0.0042$ ). Steel-Dwass (vehicle vs. healthy:  $*p = 0.043$ ; 0.1 mg/kg vs. healthy:  $*p = 0.012$ ; 0.3 mg/kg vs. healthy:  $*p = 0.023$ ). Vehicle:  $n = 17$  VEPs from 9 probes from 3 mice, 0.1 mg/kg:  $n = 27$  VEPs from 14 probes from 5 mice, 0.3 mg/kg:  $n = 13$  VEPs from 9 probes from 3 mice, healthy:  $n = 6$  VEPs from 3 probes from 2 mice. n.s. not significant,  $*p < 0.05$ ,  $***p < 0.001$ ; median, IQR (box), min./max. (whiskers) in (**A-D**); data points color-coded by mouse in A-D; two-sided statistical tests. See Supplementary Data 1 for statistical details and Source Data file for source data. VEP=visual evoked potential.

Interestingly, while remyelination therapy was incredibly effective in augmenting oligodendrocyte gain in mice with moderate or severe demyelination, thyromimetic treatment did not substantially impact oligodendrocyte gain in mice with mild demyelination (Fig. 4A). Why is remyelination therapy less effective at low oligodendrocyte loss levels? Previous studies have indicated that the survival of differentiating OPCs is approximately 20% in healthy adult mouse cortex<sup>41</sup>. One possibility is that during mild demyelination, a similarly low rate of survival could substantially dampen the effects of therapeutic-induced OPC differentiation on oligodendrocyte gain, acting as a safeguard against excessive remyelination. Future investigation into OPC differentiation and survival rates during remyelination will be critical to more fully understand this finding and other intricacies of endogenous and therapeutic-induced remyelination.

In comparing two remyelinating compounds, we observed differences in the timing of their effects on oligodendrocyte gain. 0.3 mg/kg LL-341070 induced a profound but transient increase in oligodendrocyte gain rate during the first half of its administration (Fig. 3I, J), while 10 mg/kg clemastine had a subtler impact that was most pronounced post-administration (Fig. 5D, E). While future comparisons between remyelination therapies should study multiple dosing strategies for each drug, these findings indicate that thyromimetics like LL-341070, which have historically had low tolerability when tested clinically<sup>74</sup>, may still be very effective in better-tolerated short-duration treatments. Preclinical work should carefully evaluate the safety profile of LL-341070 considering these findings. The enduring effect of clemastine on oligodendrocyte gain rate beyond the treatment period (Fig. 5D) is unlikely to be entirely explained by residual drug since clemastine is cleared fairly rapidly<sup>75,76</sup>. More likely, clemastine induces OPC differentiation during the treatment period, but as differentiating OPCs take several days to mature<sup>77</sup>, we first observe EGFP expression in some cells during the post-treatment period. The temporally limited impact of high dose LL-341070 treatment could have several explanations. First, TR $\beta$  could be inactivated with prolonged agonism. However, this is unlikely as there are sustained gene expression changes after three weeks of LL-341070 administration in rats exposed to cuprizone (Supplementary Fig. 6E–H). Second, LL-341070 could restore sufficient numbers of oligodendrocytes within the first 1.5 weeks to preclude the need for more. However, we found that a drive to restore oligodendrocyte number does not control oligodendrocyte gain rate (Fig. 2A, B), and so enhanced restoration of the oligodendrocyte population ( $84 \pm 3$  (SEM) % with 0.3 mg/kg LL-341070 at 1.5 weeks) should not inhibit future gain. Third, the high magnitude of differentiation induced by LL-341070 could cause a depletion in the OPC pool or deplete a subpopulation of OPCs more capable to differentiate<sup>78</sup>. Cortical OPCs maintain their density by elevating proliferation in response to differentiation events<sup>77</sup> but it is currently unknown how OPC numbers and dynamics are modulated by prolonged, high magnitude differentiation rates or the duration over which such rates are sustainable. Future investigation into such questions will be important to optimize therapeutic dosing strategies for remyelination.

Several of these findings may have important implications for future therapeutic strategies, and thus it will be important to ascertain whether these findings apply to other brain regions or demyelination conditions. Compared to cortex, subcortical white matter exhibits more extensive endogenous remyelination following cuprizone<sup>79</sup>, with contribution from subventricular zone-derived neural precursors<sup>19</sup>. Meanwhile, in immune-mediated demyelination conditions, the cellular microenvironment differs substantially from that of cuprizone<sup>80</sup>. Future work should determine whether the limits of endogenous remyelination and the oligodendrocyte loss-dependent triggers described here are shared across brain regions and demyelination models.

Visual impairments are a common manifestation of demyelinating diseases such as multiple sclerosis<sup>81</sup>. Thus, we utilized high-density extracellular *in vivo* recordings in a model with preferential posterior visual demyelination (Supplementary Fig. 1) to investigate the impact of demyelination on cortical visual neuronal responses. Using Neuro-pixels probes to record from the entire visual cortical column, our recordings captured both cortical neuronal responses to direct afferent visual information and to cortical processing executed within and between superficial and deep visual cortex. Due to extensive interconnectivity of V1<sup>82</sup> and dendritic processes from all layers extending to receive inputs in superficial V1<sup>83–85</sup>, we expect responses throughout the cortical column to be impacted by the superficial V1 de/remyelination imaged in this study. V1 responses are also likely affected by the de/remyelination in deeper cortical layers and subcortical optic radiations observed via immunohistochemistry (Supplementary Fig. 1). Previous work in other cortical regions indicates that superficial cortex, deep cortex, and subcortical white matter undergo remarkably similar temporal dynamics of demyelination and remyelination in response to cuprizone, with some differences in magnitude<sup>42,79</sup>. Deep cortex demyelinate to a greater extent and remyelinate to a lesser extent than superficial cortex<sup>42,79</sup>, while white matter has enhanced regeneration compared to the cortex as a whole<sup>79</sup>. Future work manipulating myelin in specific regions within cortex could help to ascertain the relative contributions of myelin in each region to cortical visual responses.

We found that demyelination delayed the responses of individual V1 neurons to visual stimuli (Fig. 6D) but did not detect statistically significant changes in the latency of aggregated V1 activity (VEP N70; Fig. 6G). Previous studies that have found demyelination-mediated changes in VEP N70 latency have induced more severe demyelination, particularly in the anterior visual pathway<sup>26,36</sup>; in contrast, we did not observe demyelination in anterior regions (Supplementary Fig. 1). These studies also monitored VEP non-invasively in the same animals before and after demyelination<sup>27,36,59</sup>, which may be important to reduce variability given that VEPs have large inter-individual differences<sup>86</sup>. Though VEP N70 latency was unaltered, we found that demyelination altered VEP shape (Fig. 6I), perhaps due to the added dependence of VEP shape on cortical processing in addition to input from the anterior visual pathway. Intriguingly, this finding suggests that cortical demyelination may contribute to the well-described changes in VEP shape in multiple sclerosis patients<sup>87</sup>.

After seven weeks of remyelination, animals treated with LL-341070 reached a plateau of functional recovery of visual response metrics similar to healthy levels (Fig. 7A–D). Furthermore, the high dose of this remyelination therapy shortened the restoration of V1 neuronal function to three weeks (Fig. 6E, J). These findings are in line with previous reports indicating that remyelination can restore demyelination-mediated deficits in stimulus-evoked neuronal latencies leading to behavioral improvements<sup>27,36</sup>, highlighting the imperative to bring remyelinating therapeutics to patients. Remyelination restores conduction properties<sup>2</sup>, synaptic transmission<sup>88</sup>, and neuron excitability<sup>21,88</sup> disrupted by demyelination. But our study indicates this relationship is complex, with different aspects of neuronal visual function recovering at different times in different groups, and at different levels of regeneration of oligodendrocytes and myelin. Restoration of the cortical oligodendrocyte population to below baseline levels and of myelin to baseline levels correlated to restored visual neuronal latency in mice treated with high dose LL-341070 at three weeks, but comparable levels of remyelination did not recover neuronal latencies in low dose-treated mice at three weeks or vehicle-treated mice at seven weeks (Fig. 7E), indicating additional factors are involved. A potential contributor to these different functional outcomes is the timing with which these groups regenerated oligodendrocytes. High dose LL-341070 accelerated regenerative

oligodendrogenesis specifically during the first 1.5 weeks of remyelination, generating more oligodendrocytes than both low dose- and vehicle-treated groups by 1.5 weeks (Figs. 3H, J, 7E). Earlier remyelination could have several benefits for axonal conduction. First, new nodes and internodes would have sufficient time to mature. New sheaths require several days to grow to their mature lengths<sup>21,89</sup> and compact their myelin<sup>90</sup>. Nodal assembly and maturation must also occur, with sodium channels present transiently during repair (Na<sub>v</sub>L2) being replaced by the mature CNS isoform (Na<sub>v</sub>L6)<sup>91</sup>.

Second, rapid recovery of oligodendrocytes may prevent the disruption of axons from occurring in the first place. Nodal disassembly<sup>42,91</sup>, loss or functional disruption of synapses<sup>88,92–94</sup>, and axonal pathology<sup>5,95</sup> become progressively more severe with longer periods of demyelination, but may be prevented with timely remyelination. In particular, rapid remyelination of previously demyelinated axonal segments, which frequently occurs in cortical remyelination<sup>13,42,44</sup>, may enable the reutilization of residual nodal architecture to expedite recovery of saltatory conduction. Furthermore, though synaptic and axonal pathologies are not pronounced at the end of a 3–3.5-week cuprizone exposure<sup>93</sup> (Supplementary Fig. 2C, E), it is possible they would emerge if remyelination is insufficient or delayed.

Third, rapid remyelination may better preserve the spatial pattern of myelin. New oligodendrocytes formed during remyelination myelinate both demyelinated axon segments and previously unmyelinated regions, leaving some regions demyelinated and resulting in rearrangement of the myelin landscape<sup>21,42,44</sup>. Interestingly, it is the more heavily myelinated axons that are prioritized for remyelination<sup>13,42,44</sup>, perhaps indicating an outsized functional importance to their remyelination. Furthermore, these axons become remyelinated more quickly than other axons<sup>13</sup>, suggesting signaling present shortly following their demyelination (e.g. residual nodal components, axonal “myelinate me” signals) directs their remyelination by new oligodendrocytes. But even so, approximately 20% of these axon segments are not remyelinated after numerous weeks<sup>13,42,44</sup>. Accelerating remyelination to ensure sufficient oligodendrocytes present in the period following their demyelination may facilitate more complete remyelination of these heavily myelinated axons, perhaps enabling recovery of neuronal responses at lower levels of remyelination. Future interrogation of how the magnitude and timing of demyelination and remyelination alters the ultrastructure and function of individual axons as well as broader network and behavioral recovery will be important for developing optimal strategies for remyelination therapies.

## Methods

### Animals

All animal experiments were approved by the Institutional Animal Care and Use Committee (IACUC) of the University of Colorado Anschutz Medical Campus (Protocol 00056). Animals were housed in sex-segregated individually ventilated cages, in groups up to five. Food and water were provided ad libitum. The room was kept at 72 °F ± 2 °F temperature with 50 ± 20% humidity and was on a 14 h light 10 h dark cycle. The Tg(Mobp-EGFP)INI<sup>Gsat</sup>/Mmucd mouse line (referred throughout the text as *Mobp-EGFP*; MGI:4847238) was described previously<sup>41,96</sup>. *Mobp-EGFP* mice were from a C57BL/6 genetic background. Both male and female *Mobp-EGFP* hemizygous mice were used for experiments, with sex being distributed between treatment groups. No evidence of sexual dimorphism was observed (Supplementary Fig. 16A–C).

### Genotyping

Genotyping for *Mobp-EGFP* was performed from genomic DNA, using genotyping primers F: 5' GGTTCCTCCCTCACATGCTGTTT 3' and R: 5' TAGCGGCTGAAGCACTGCA 3' and PCR conditions of 94 °C for 4 min, [94 °C for 30 s, 73–68 °C (0.5 °C decrease per cycle) for 30 s and 72 °C

for 30 sec] for 10 cycles, (94 °C for 30 s, 68 °C for 30 s and 72 °C for 30 sec) for 28 cycles, and 72 °C for 7 min, yielding a ~300 bp band.

### Cranial window implantation surgery

6–8-week-old mice were anesthetized with isoflurane inhalation (induction, 5%; maintenance, 1.5–2.0%, mixed with 0.5 L/min O<sub>2</sub>) and kept at 37 °C body temperature with a thermostat-controlled heating plate. After removal of the skin over the right cerebral hemisphere, the skull was cleaned and a 2 × 2 mm region of skull centered over the primary visual cortex (1.5 mm anterior to lambda–0.5 mm posterior to lambda and 1.5–3.5 mm lateral to bregma) was removed using a high-speed dental drill. A piece of cover glass (VWR, No. 1) was then placed in the craniotomy and sealed with Vetbond (3M) and then dental cement (C&B Metabond). A 5 mg/kg dose of carprofen was subcutaneously administered before awakening. For head stabilization during in vivo imaging, a custom metal plate with a central hole was attached to the skull with dental cement.

### Remyelination therapies

LL-341070 was provided by Autobahn Therapeutics as a solution in 1% 1-methyl-2-pyrrolidone (Sigma 270458) and 1% Kolliphor HS 15 (Sigma 42966) to a final concentration of 20 µg/ml or 60 µg/ml. Inquiries concerning LL-341070 should be directed to ethan.hughes@cuanschutz.edu. High dose, low dose, and vehicle solutions for LL-341070 were provided blinded to the experimenters and were unblinded following image or electrophysiological analysis. Clemastine fumarate (Tocris 1453) was solubilized in a 10% DMSO solution to a final concentration of 1 mg/ml. Solutions of clemastine fumarate and its vehicle were blinded in-house by personnel unaffiliated with the project and were unblinded following image analysis. Remyelination therapies or respective vehicles were administered once daily for three weeks by gavage at 10 mL/kg for clemastine and 5 mL/kg for LL-341070, resulting in doses of 0.1 mg/kg or 0.3 mg/kg for LL-341070 and 10 mg/kg for clemastine. Mice treated with LL-341070 and clemastine or their respective vehicles were run in simultaneous cohorts by the same experimenters and in some instances were run in the same cohort. Mice were randomly allocated to blinded groups either prior to or during cuprizone treatment. In some instances, the level of oligodendrocyte loss during cuprizone was assessed prior to mouse allocation to attempt to ensure an even distribution of oligodendrocyte loss levels between blinded groups. Since we did not observe notable differences between untreated and vehicle-treated mice (Supplementary Fig. 3), these mice were combined to study endogenous remyelination (Figs. 1, 2).

### Cuprizone-mediated demyelination

Demyelination was induced in 9–10-week-old mice using 0.2% Bis(cyclohexanone)oxaldihydrazone (cuprizone; Sigma C9012 or Sigma 14690), stored in a glass desiccator at 4 °C. Cuprizone was added to powdered chow (Envigo T.2918 M.15), mixed for ~10 min to ensure homogeneity, and provided to mice in custom feeders (designed to minimize exposure to moisture) for 24–25 days on an ad libitum basis. Feeders were refilled every 2–3 days, and fresh cuprizone chow was prepared weekly. Healthy mice received normal powdered chow in identical feeders. Regular chow was removed and powdered chow was introduced 2–3 days before cuprizone to ensure acclimation to the powdered food. Cages were changed weekly to avoid build-up of cuprizone chow in bedding, and to minimize reuptake of cuprizone chow following cessation of diet via coprophagia. Sex, change in mouse weight, and inter-cohort differences could not explain the variability of oligodendrocyte loss found in our study (Supplementary Fig. 16A, D, E).

### Two-photon imaging

In vivo imaging sessions began three weeks post-surgery and took place 1–3 times per week (Fig. 1A, B). During imaging sessions, mice

were anesthetized with isoflurane and immobilized by attaching the head plate to a custom stage. Images were collected using a Zeiss LSM 7MP microscope equipped with a BiG GaAsP detector using a mode-locked Ti:sapphire laser (Coherent Ultra) tuned to 920 nm. The average power at the sample during imaging was 5–30 mW. Vascular and cellular landmarks were used to identify the same cortical region over longitudinal imaging sessions. *Mobp*-EGFP image stacks were acquired using a Zeiss W plan-apochromat  $\times 20/1.0$  NA water immersion objective giving a volume of  $425 \mu\text{m} \times 425 \mu\text{m} \times 336 \mu\text{m}$  ( $1024 \times 1024$  pixels; corresponding to layers I–III, 0–336  $\mu\text{m}$  from the meninges) from the cortical surface.

### Image processing and analysis

During data analysis, experimenters were blinded to the experimental groups. For presentation in figures, image brightness and contrast levels were adjusted for clarity. Images were analyzed using ImageJ (v1.54 f)<sup>97</sup> unless otherwise specified.

For quantification of nodes of Ranvier, three fields of view of 10,000  $\mu\text{m}^2$  were quantified manually per animal. For the DegenTag analysis, blood vessels stained non-specifically by the anti-mouse secondary antibody were first cropped out using ilastik<sup>98</sup>. For analyses of *Mobp*-EGFP cell density, axon degeneration and glial reactivity, immunohistochemistry images were quantified in the entire region of interest in both hemispheres using 3D hysteresis thresholding from the 3D Suite plugin (ImageJ)<sup>99</sup> for segmentation. For analysis of retinal ganglion cells, 8 fields of view for a total area of 0.2  $\text{mm}^2$  were quantified from each whole-mounted retina.

Longitudinal two-photon in vivo 4D images were registered iteratively with Poorman3Dreg plugin for X/Y registration (ImageJ v1.46r) followed by Correct3D drift plugin (EGFP channel, rigid body registration, 30x30x20 pixels X/Y/Z; ImageJ v1.54 f)<sup>100</sup>. For analysis of new oligodendrocyte sheaths, Correct3D drift was repeated on a smaller ROI containing cell of interest.

Oligodendrocyte cell tracking was performed manually (ImageJ v1.51p). A custom ImageJ script<sup>41</sup> enabled recording of oligodendrocyte state (new, lost, or stable EGFP+ soma) across timepoints.

Myelin sheath tracing was performed using Simple Neurite Tracer (ImageJ) in order to derive length measurements in three dimensions. New oligodendrocytes selected for sheath analysis had the following requirements: 1. Soma must be at least 85  $\mu\text{m}$  from FOV edge; 2. Soma must be at least 170  $\mu\text{m}$  from another oligodendrocyte soma new at the same timepoint; 3. New sheaths must be clearly visible for at least two timepoints, i.e. oligodendrocytes new at the last timepoint were not analyzed. Sheaths were traced at either the first or second timepoint after the oligodendrocyte appeared (depending on reporter expression and image clarity) and compared to the two timepoints prior to cell appearance. Importantly, *Mobp*-EGFP+ cells appear with all their sheaths already formed as the reporter expresses later in oligodendrocyte generation. Sheaths were considered as belonging to the new oligodendrocyte if they appeared at the same timepoint and were in the region of the new cell. New oligodendrocytes and their sheaths have brighter reporter expression than pre-existing oligodendrocytes. We observed a few instances of putative simultaneous demyelination and remyelination<sup>13</sup>, wherein a pre-existing sheath appeared to brighten at the same timepoint as the new cell appeared. Typically, the new process connecting the brightened sheath back to the new oligodendrocyte soma could be observed; in such cases, the brightened sheath was traced and counted as belonging to the new oligodendrocyte.

### Immunohistochemistry

Mice were anesthetized with an intraperitoneal injection of sodium pentobarbital (100 mg/kg body weight) and transcardially perfused with 4% paraformaldehyde in 0.1M phosphate buffer (pH 7.0–7.4). Optic nerves and brains were postfixed in 4% paraformaldehyde

overnight at 4 °C, transferred to 30% sucrose solution in PBS (pH 7.4) and stored at 4 °C until processing. Tissue was positioned in cryomolds with Tissue-Tek OCT, frozen, and sections were obtained using a cryostat (optic nerve and brain sections were 10  $\mu\text{m}$  and 40  $\mu\text{m}$  thick, respectively). For optic nerves, immunostaining was performed with sections on a slide and sections were first permeabilized with acetone for 5 min, while brain sections were immunostained using a free-floating method. Sections were blocked (5% normal donkey serum, 0.3% Triton X-100 in PBS, pH 7.4) for 1 h at room temperature, then incubated overnight at 4 °C with primary antibody followed by washes and secondary antibody incubation for 1 h at room temperature. Primary and secondary antibodies were diluted in the blocking buffer. Primary antibodies and dilutions were Rabbit anti-Caspr 1:500 (Abcam ab34151; RRID:AB\_869934), Chicken anti-pan-Nfsc 1:500 (R&D Biosystems AF3235; RRID:AB\_10890736), Rat anti-PLP 1:500 (gift from Dr. Wendy Macklin), Mouse anti-Degenotag 1:500 (Encor Biotechnology MCA-1D44; RRID:AB\_2923483), Mouse anti-GFAP 1:1000 (Sigma G3893; RRID:AB\_477010), Rabbit anti-S100 $\beta$  1:500 (Abcam AB52642; RRID:AB\_882426), and Rabbit anti-P2RY12 1:1000 (Anaspec AS-55043A). Secondary antibodies (diluted 1:500) were Alexa Fluor 488 Donkey anti-chicken IgY (Jackson ImmunoResearch Laboratories 703-545-155), Alexa Fluor 568 Donkey anti-rabbit IgG (Thermo Fischer A10042), Alexa Fluor 568 Goat anti-rat IgG (Thermo Fischer A11077), Alexa Fluor 568 Donkey anti-mouse IgG (Thermo Fischer A11004), and DyLight 405 Donkey anti-mouse IgG (Jackson ImmunoResearch Laboratories 715-475-150). Sections were mounted on slides with Vectashield antifade reagent (Vector Laboratories). Images were acquired using a laser-scanning confocal microscope (Leica SP8) at a magnification of 63X for nodal stainings and 20X or 25X for the remaining analyses.

Retinas were prepared and stained using a protocol adapted from<sup>101</sup>. In brief, retinas were dissected out of the optic cup, fixed with 4% PFA for 30 min at RT and washed with PBS four times: flash (adding 500  $\mu\text{L}$  PBS to the tube, inverting 3 times and then proceeding to the next wash), 15 min, 1 h,  $\geq 2$  h. Retinas were then subjected to a similar series of washes with 0.5% PBST (0.05% Triton X-100), and incubated in blocking buffer (1% BSA, 10% normal donkey serum, 0.5% triton x-100) for  $\geq 3$  h. Staining was performed using a free-floating method. Primary antibody guinea pig anti-RBPMS (PhosphoSolutions 1832-RBPMS; RRID:AB\_2492226) was diluted 1:100 in reaction buffer (1% BSA, 3% normal donkey serum, 0.05% triton X-100) and retinas were incubated with this solution at RT in a nutating mixer for 5 days. After a series of washes with PBST, retinas were incubated with FITC Donkey anti-guinea pig diluted 1:200 in reaction buffer at 4 °C on a nutating mixer overnight. After a series of washes with PBST followed by washes with PBS, retinas were mounted flat on slides with the RGC layer facing up (cover slide side) by making 4 symmetrical cuts on the retina and using ProLong anti-fade mounting medium. The entire retinas were imaged as tiles on an Olympus DSU spinning disc microscope with a 20X objective, and images were stitched together with an ImageJ macro.

### Visual stimulation

Stimuli were displayed on the inner surface of a custom-designed spherical dome enclosure (Supplementary Fig. 12A). The enclosure was a clear 24" diameter acrylic sphere (California Quality Plastics, Ontario, CA) coated with a custom UV-reflective paint. The paint had 50% absorbance to reduce interference caused by internal reflections and reflection was spectrally flat from 350 to 600 nm (Twilight Labs Inc., Grand Forks, ND). The animal was placed on a horizontal disc suspended near the center of the sphere, head-fixed such that it could run freely, and positioned with the right eye at the center of the sphere. This created a spherical coordinate system with the viewing eye at the origin; based on previous measurements the optical axis projects to 22° in elevation and 60° in azimuth in the dome coordinate system. A custom digital light processing (DLP) projector (DLI Innovations,



Austin, TX) with mouse photoreceptor-optimized LED sources placed outside of the enclosure projected, at a refresh rate of 60 Hz, through a small opening in the dome onto a silver-coated aluminum mirror (Wagner Collaborative Metal Works, Milwaukee, WI) suspended beneath the mouse platform. Visual stimuli covered 200° in azimuth and 100° in elevation. Visual stimuli were generated on a PC using custom written software based on the PsychoPy (<http://www.psychopy.org>) platform. Flashed stimuli consisted of 50 msec temporary increases (bright flash) or decreases (dark flash) in full-field luminance,  $-1.8 \text{ cd/m}^2$  from a mean luminance of  $3.6 \text{ cd/m}^2$ .

### In vivo electrophysiology

To record from neuronal populations across primary visual cortex (V1) we used three Neuropixels<sup>102</sup> probes simultaneously. These are high-density electrophysiology probes with 384 contiguous channels on a single shank covering 3.84 mm. Immediately before the recording, the animals were anesthetized, the cranial window was removed, and a partial durotomy was performed to allow for probe insertion. After head-fixation inside a visual stimulus environment, probes were inserted through the opening in the skull. Recordings were grounded to the animal. Following insertion, the exposed skull was covered with 1–2% agar to improve recording stability and maintain brain health. For all recordings, several hundred channels were left outside of the brain but within the covering agar to facilitate data-driven probe localization. The probe was allowed to settle for at least 15, but typically 30 min, before responses were recorded. Each probe averaged  $196 \pm 165$  (SD) visual cortical neurons per recording. A post-hoc assignment of both unit depth and cortical layer was made by taking the distance between the center of the waveform amplitude distribution along the shank and the channel estimated at just beyond the pial surface. Neurons were recorded from all cortical layers, though distributions were biased towards deeper regions (Supplementary Fig. 12D).

### In vivo electrophysiology: spike sorting and pre-processing

Electrophysiological data from each channel was recorded in two bands: a “spike” band sampled at 30 kHz and hardware filtered at 300–10,000 Hz, and a “field potential” band sampled at 2.5 kHz and hardware filtered at 0.1–500 Hz (Supplementary Fig. 7C).

To recover the spike times from individual neurons recorded in the spike band, we used a workflow that included algorithmic and manual refinement steps. We began with spike time extraction and putative single unit isolation using Kilosort, and manually refined the results using phy ([github.com/cortexlab/phy](https://github.com/cortexlab/phy)). During manual refinement, most decisions were merging of clusters that had been algorithmically split due to drift in amplitude on the timescale of the entire recording; in addition, the first spikes in a burst also needed to be manually merged. Each unit was tagged as multi-unit (MUA) or single-unit based on the waveform and shapes of neighboring waveforms and the middle few milliseconds of the spike time auto-correlograms. For each recording, the quality of isolation of each unit was quantified using several metrics: maximum signal-to-noise, purity of the auto-correlogram, and distance of the mean waveform from other units in both feature and waveform space. These metrics were combined into a single quality metric using a Fisher’s linear discriminant projection based on the manual labels. Finally, the depth of each unit from the pial surface was calculated based on features of the neural data. We calculated the power in a range of frequency bands for each channel for a short epoch. The distribution of several bands revealed features of the underlying structure; from the alpha-band (8–14 Hz), we were able to identify the first channel above the pial surface. This channel served as the reference channel for measuring the depth of each unit. The center of each unit was calculated based on the mean waveform, weighted by the amplitude of the waveform on each channel. Using the spike trains

from these large populations of single neurons, we compare latencies to visual responses between conditions.

To analyze visually evoked potentials, we computed average potentials on each of the hundreds of electrodes in the visual cortex. Unfiltered local field potentials were trial-averaged to generate evoked potentials; a linear sub-array of channels corresponding to those in visual cortex was selected from the recorded data. Since visual evoked potentials (VEPs) are usually recorded non-invasively from scalp electrodes placed over the occipital region, electrical activity from superficial cortex is overrepresented in these recordings. To match this effect for comparison to clinical VEPs, we applied a log-weight according to depth of the electrode and summed all the evoked potentials. Because nominal amplitude values can be affected by the degree of tissue damage caused by probe placement, as well as the geometry of the electrode relative to large potential sources such as the apical dendrites of large neurons, VEP amplitude data was normalized by the standard deviation of VEP signals preceding the stimuli for each Neuropixels probe.

To calculate the shape distortion metric, we first averaged the computed VEP of healthy animals to create a VEP shape template. We then calculated a point-by-point spatial distance correlation between the conditional VEPs and the VEP shape template (*scipy.spatial.distance.correlation*). Since this is a comparative measure that is bounded between 0 and 2, VEP responses to bright and dark flash were considered to be independent and were analyzed together.

The VEP signal was manually inspected by an investigator blinded to the experimental conditions, and signals deemed to have low quality were excluded from further analyses.

### Thyroid hormone receptor selectivity assay

Commercially available luciferase reporter assays were performed by INDIGO Biosciences (State College, PA), as requested by Autobahn Therapeutics. Two different HEK-derived cell lines were generated which express a TR $\alpha$  or TR $\beta$  hybrid in which the native N-terminal DNA binding domain (DBD) has been replaced with that of the yeast Gal4DBD. The reporter gene, firefly luciferase, is functionally linked to the Gal4 upstream activation sequence (UAS). A suspension of either TR $\alpha$  or TR $\beta$  reporter cells was prepared in INDIGO’s cell recovery medium (CRM; containing 10% charcoal-stripped FBS) and dispensed into assay plates and preincubated for 6 h. Cells were treated with LL-341070 or LL-341070A (in 0.4% DMSO) in duplicates with drug concentrations ranging from 0.031 to 10000 nM in half-log dilutions. Cells were treated with T<sub>3</sub> in (0.1% DMSO) in concentrations ranging from 0.023 to 50 nM in half-log dilutions. 22–24 h after treatment, media was removed and replaced with luciferase detection reagent and read with a luminometer. Data were normalized to vehicle-treated wells and fit with a 4-parameter logistic regression using Prism (GraphPad) with the bottom of the curve set to 1. LL-341070A was evaluated in two independent experiments with <2.2-fold difference in potency between the different experiments; LL-341070 was evaluated in a single study. To calculate TR $\beta$ -selectivity, the ratio of the EC<sub>50</sub> in the TR $\alpha$  to TR $\beta$  assay was evaluated and normalized by that same ratio observed for T<sub>3</sub> in the same experiment. T<sub>3</sub> is equipotent against both TR isoforms in cell-free systems; thus, normalizing the ratio for that observed for T<sub>3</sub> reduces the impact of the artificial nature of using two different cell lines.

### In vitro OPC differentiation

OPC differentiation assays were performed by Renovo Neural (Cleveland, OH) on a fee-for service basis for Autobahn Therapeutics. OPCs were isolated from brains of E14.5 *Plp-EGFP* C57Bl/6 mice. Cells were cultured in Renovo’s “Neurosphere media”. Once confluent, neurospheres were dissociated into single cells and seeded onto coated 96-well plates at ~6000 cells/well. Cells were cultured in Renovo’s OPC media for two days, when the majority of cells display typical bipolar

OPC morphology and are positive for NG2. Media was then replaced with Renovo's Treatment media and treated for 5 days with either vehicle (0.1% DMSO), various concentrations (1, 3, 10, 30, 100, 300, 1000, and 3000 nM) of LL-341070A, or 10 ng/mL (15.4 nM) T<sub>3</sub> as a positive control. N = 6 wells were treated per condition. Maximum concentration of DMSO was 0.1% after final dilution. Media was replaced once at 48 h. On day 5, cells were fixed with 4% paraformaldehyde and stained for MBP (Millipore #MAB386) and with Hoechst 33342 to visualize cell nuclei. Cells were imaged in a Cellomics VTI Array Scanner with 20 images captured from each well. Computer algorithms developed at Renovo Neural were used to identify and count MBP+ OLS, total number of Hoechst 33342+ cells, and pyknotic nuclei. Data were reported as % live cells positive for MBP staining.

### Rat thyroid hormone target gene expression

All components of this assay were performed by Autobahn Therapeutics. Adult (225–250 g) female Wistar rats (Charles River Laboratories) were placed on a diet containing 0.6% cuprizone for 3 weeks. Following cuprizone, rats (n = 10 per group) were dosed with either vehicle or 0.03 or 0.1 mg/kg LL-341070 by oral gavage daily for 3 weeks. 4 h after the final dose, animals were anesthetized by isoflurane and the brain was harvested. Cerebellum, corpus callosum, and cortex were removed for other analyses and the remainder of the brain was placed in cold RNALater and frozen at -20 °C. Brain samples were processed for gene expression using a Nanostring-based hybridization analysis (NanoString, Seattle, WA). For RNA extraction, tissues were homogenized using a bead homogenizer in TRIzol Reagent, catalog # 15596026 (ThermoFisher Scientific), and RNA was extracted according to manufacturer's protocols and purified using Econospin RNA Mini Spin Columns for RNA (EPOCH Life Sciences, Missouri City, TX, catalog #1940-250) following manufacturer's protocols. Specific gene probes were designed by NanoString Bioinformatics using an identified target sequence based on the NCBI Reference Sequence (RefSeq) database. Custom probes were synthesized by Integrated DNA Technologies (IDT; Coralville, IA). mRNA expression was analyzed on an nCounter® SPRINT Profiler NanoString system using a multiplexing approach with nCounter PlexSet-12 Reagent Pack, catalog #PS-GX-PTK-12 (CSO) according to manufacturer's protocols (NanoString, Inc, Seattle, WA). Target genes were Hairless (*Hr*), Deiodinase 3 (*Dio3*) and Kruppel-like factor 9 (*Klf9*), all validated T<sub>3</sub> target genes. Glucuronidase beta (*Gusb*) and thioredoxin 2 (*Txn2*) and peptidylprolyl isomerase b (*Ppib*) were used as housekeeping genes. Expression of each individual gene is expressed as normalized counts, normalized to the geometric mean of housekeeping genes, analyzed with nSolver 4.0 software (NanoString, Inc, Seattle, WA).

### Statistics and modeling

Summarized statistical information is present in the legend of each figure. Detailed statistical information is in Supplementary Data 1. Sample sizes were not predetermined using statistical methods, but were comparable to relevant publications<sup>21,41</sup>. Experimental groups were replicated in multiple cohorts with multiple experimental groups per cohort. For longitudinal imaging experiments, treatment groups were repeated in the following number of cohorts: untreated = 2; LL-341070 vehicle, 0.1 mg/kg, and 0.3 mg/kg = 5; clemastine = 3; clemastine vehicle = 2; healthy = 2. For electrophysiology, treatment groups were repeated in the following number of cohorts: healthy = 1; demyelinated = 3; LL-341070 vehicle = 3; LL-341070 0.1 mg/ml = 4; and LL-341070 0.3 mg/ml = 2. Statistical analyses were conducted using JMP Pro 17 (SAS) or Prism 7 (GraphPad). Normality was assessed in all datasets using the Shapiro-Wilk test.

Normality was satisfied in all longitudinal imaging experiments, so parametric statistics were used. To compare group means, paired two-tailed Student's *t* test or ANOVA with Tukey's post hoc were used. To compare variance between different groups, the Brown–Forsythe test

was used. To investigate the relationship between two variables, simple linear regression was used; the coefficient of determination (R<sup>2</sup>) and the *p*-value of an ANOVA testing the null-hypothesis that there is no linear relationship between the tested variables were reported. Given that oligodendrocyte gain depends on the level of oligodendrocyte loss, we used an analysis of covariance with unequal slopes to take this relationship into account when testing for drug effects, wherein the dependent variable was cumulative oligodendrocyte gain (or gain rate), the independent variable was treatment, the covariate was cumulative oligodendrocyte loss, and the interaction term was cumulative oligodendrocyte loss by treatment. This analysis performs an independent linear regression of cumulative gain (or gain rate) versus cumulative loss for each treatment group, and reports whether there are significant effects on the dependent variable of the independent variable, covariate, or interaction term. The resulting graphical representation of this step displays all data points and has been presented, mostly in the Supplementary Figs., for every analysis. To compare treatment groups, post-hoc tests were used. The least square mean estimates of cumulative oligodendrocyte gain (or gain rate) (i.e. cumulative gain or gain rate corrected by cumulative loss at the average cumulative loss value of all groups) for each treatment group were compared using a post-hoc Tukey's HSD or *t*-test in JMP. The graphical representation of this step displays the least square mean and SEM for each group used in this step as well as the significant post-hoc statistical comparisons between groups.

To account for variations in baseline oligodendrocyte number, all oligodendrocyte metrics are reported as a percentage of baseline oligodendrocytes. The following metrics were derived from the raw oligodendrocyte counts:

$$\text{Cumul. lost or new OLS (\%)} = \frac{\text{Cumul. no. of lost or new OLS}}{\text{No. of baseline OLS}} \quad (1)$$

$$\text{OL no. (\%)} = \frac{\text{No. of OLS}}{\text{No. of baseline OLS}} \quad (2)$$

$$\text{OL loss or gain rate (\%/day)} = \frac{\left(\frac{\text{No. of lost or new OLS from } t_1 \text{ to } t_2}{\text{No. of baseline OLS}}\right)}{t_2 - t_1 \text{ days}} \quad (3)$$

To model the continuous dynamics of oligodendrocyte gain or loss, we used Gompertz three-parameter modeling:

$$ae^{(-e^{-(b(\text{time}-c)})} \quad (4)$$

where:

- a* = asymptote
- b* = curve's growth rate
- c* = inflection point

Only mice with imaging data out to three weeks were modeled.

For Fig. 2, we used a quintic polynomial curve to model the variation in oligodendrocyte population (% of baseline) throughout demyelination and remyelination. Only mice with imaging data out to three weeks were modeled. Quintic polynomial curves fit the data well from -14 to 18 days, and so the output was only used from this period.

Oligodendrocyte gain and loss rates in Fig. 2 were obtained from the first derivative of the modeled dynamics of oligodendrocyte gain or loss. Maximum oligodendrocyte gain rate (Figs. 3I and 5E) was the oligodendrocyte gain rate at the inflection point of the modeled oligodendrocyte gain curve.

Total myelin sheath number (Fig. 4J) and length (Supp. Fig. 10E) were estimated with the following assumptions: 1. Oligodendrocytes present at baseline in treated or healthy mice had a number and length of myelin sheaths equivalent to the mean of new oligodendrocytes in healthy mice (43.38 sheaths per oligodendrocyte and 2911.34 μm total

myelin length); 2. Loss of an oligodendrocyte resulted in loss of all its myelin sheaths; 3. New oligodendrocytes had the average number of myelin sheaths and length experimentally determined for their respective groups (Vehicle = 52.06 myelin sheaths with a total length of 3514.78  $\mu\text{m}$ , 0.1 mg/kg = 52.64 myelin sheaths with a total length of 3985.54  $\mu\text{m}$ , 0.3 mg/kg = 51.71 myelin sheaths with a total length of 3278.09  $\mu\text{m}$ , Healthy = 43.38 myelin sheaths with a total length of 2911.34  $\mu\text{m}$ ). This estimate does not factor in potential sheath loss or gain by surviving oligodendrocytes, which we expect to have only a minimal contribution to total myelin levels. Myelin sheath loss from surviving oligodendrocytes is likely greater than sheath gain, probably resulting in a slight overestimation of myelin levels.

For the electrophysiology results, normality was violated; therefore, we used nonparametric tests: Wilcoxon signed-rank test for comparisons between two groups and Kruskal-Wallis test followed by Steel-Dwass post-hoc tests to compare more than two groups.

For data visualization, all error bars represent the standard error of the mean, all bar graphs denote means and all box plots illustrate medians and IQRs unless otherwise specified. Significance was determined by  $p < 0.05$ , except when a Bonferroni correction was used for multiple comparisons (Fig. 2, indicated in legend and Supplementary Data 1).

### Reporting summary

Further information on research design is available in the Nature Portfolio Reporting Summary linked to this article.

### Data availability

Source data are provided in the Source Data file. All data that support the findings will be shared on an unrestricted basis; requests should be directed to the corresponding authors. Source data are provided with this paper.

### Code availability

Data analysis notebooks and scripts for electrophysiology data are available on github (<https://github.com/denmanlab/remyelination>).

### References

- McDonald, W. I. & Sears, T. A. Effect of Demyelination on Conduction in the Central Nervous System. *Nature* **221**, 182–183 (1969).
- Smith, K. J., Blakemore, W. F. & McDonald, W. I. Central remyelination restores secure conduction. *Nature* **280**, 395–396 (1979).
- Irvine, K. A. & Blakemore, W. F. Remyelination protects axons from demyelination-associated axon degeneration. *Brain* **131**, 1464–1477 (2008).
- Mei, F. et al. Accelerated remyelination during inflammatory demyelination prevents axonal loss and improves functional recovery. *Elife* **5**, e18246 (2016).
- Duncan, G. J. et al. Remyelination protects neurons from DLK-mediated neurodegeneration. *Nat. Commun.* **15**, 9148 (2024).
- Sen, M. K., Mahns, D. A., Coorssen, J. R. & Shortland, P. J. Behavioural phenotypes in the cuprizone model of central nervous system demyelination. *Neurosci. Biobehav. Rev.* **107**, 23–46 (2019).
- Kister, I. et al. Natural History of Multiple Sclerosis Symptoms. *Int. J. MS Care* **15**, 146–156 (2013).
- Popescu, B. F. G. H. & Lucchinetti, C. F. Pathology of Demyelinating Diseases. *Annu. Rev. Pathol.: Mechanisms Dis.* **7**, 185–217 (2012).
- Armstrong, R. C., Mierzwa, A. J., Marion, C. M. & Sullivan, G. M. White matter involvement after TBI: Clues to axon and myelin repair capacity. *Exp. Neurol.* **275**, 328–333 (2016).
- Papastefanaki, F. & Matsas, R. From demyelination to remyelination: The road toward therapies for spinal cord injury. *Glia* **63**, 1101–1125 (2015).
- Marin, M. A. & Carmichael, S. T. Mechanisms of demyelination and remyelination in the young and aged brain following white matter stroke. *Neurobiol. Dis.* **126**, 5–12 (2019).
- Nasrabady, S. E., Rizvi, B., Goldman, J. E. & Brickman, A. M. White matter changes in Alzheimer's disease: a focus on myelin and oligodendrocytes. *Acta Neuropathologica Commun.* **6**, 22 (2018).
- Chapman, T. W., Olveda, G. E., Bame, X., Pereira, E. & Hill, R. A. Oligodendrocyte death initiates synchronous remyelination to restore cortical myelin patterns in mice. *Nat. Neurosci.* **26**, 555–569 (2023).
- Hill, R. A., Li, A. M. & Grutzendler, J. Lifelong cortical myelin plasticity and age-related degeneration in the live mammalian brain. *Nat. Neurosci.* **21**, 683–695 (2018).
- Mainero, C., Treaba, C. A. & Barbuti, E. Imaging cortical lesions in multiple sclerosis. *Curr. Opin. Neurol.* **36**, 222–228 (2023).
- Chard, D. T. et al. Mind the gap: from neurons to networks to outcomes in multiple sclerosis. *Nat. Rev. Neurol.* **17**, 173–184 (2021).
- Duncan, G. J. et al. Myelin regulatory factor drives remyelination in multiple sclerosis. *Acta Neuropathol.* **134**, 403–422 (2017).
- Tripathi, R. B., Rivers, L. E., Young, K. M., Jamen, F. & Richardson, W. D. NG2 Glia Generate New Oligodendrocytes But Few Astrocytes in a Murine Experimental Autoimmune Encephalomyelitis Model of Demyelinating Disease. *J. Neurosci.* **30**, 16383–16390 (2010).
- Xing, Y. L. et al. Adult neural precursor cells from the sub-ventricular zone contribute significantly to oligodendrocyte regeneration and remyelination. *J. Neurosci.* **34**, 14128–14146 (2014).
- Moyon, S., Holloman, M. & Salzer, J. L. Neural stem cells and oligodendrocyte progenitor cells compete for remyelination in the corpus callosum. *Front Cell Neurosci.* **17**, 1114781 (2023).
- Bacmeister, C. M. et al. Motor learning promotes remyelination via new and surviving oligodendrocytes. *Nat. Neurosci.* **23**, 819–831 (2020).
- Duncan, I. D. et al. The adult oligodendrocyte can participate in remyelination. *Proc. Natl Acad. Sci. USA* **115**, E11807–E11816 (2018).
- Mezydło, A. et al. Remyelination by surviving oligodendrocytes is inefficient in the inflamed mammalian cortex. *Neuron* **111**, 1748–1759.e8 (2023).
- Neely, S. A. et al. New oligodendrocytes exhibit more abundant and accurate myelin regeneration than those that survive demyelination. *Nat. Neurosci.* **25**, 415–420 (2022).
- Chang, A., Tourtellotte, W. W., Rudick, R. & Trapp, B. D. Remyelinating oligodendrocytes in chronic lesions of multiple sclerosis. *N. Engl. J. Med.* **346**, 165–173 (2002).
- Goldschmidt, T., Antel, J., König, F. B., Brück, W. & Kuhlmann, T. Remyelination capacity of the MS brain decreases with disease chronicity. *Neurology* **72**, 1914–1921 (2009).
- Cordano, C. et al. Validating visual evoked potentials as a pre-clinical, quantitative biomarker for remyelination efficacy. *Brain* **145**, 3943–3952 (2022).
- Sozmen, E. G. et al. Nogo receptor blockade overcomes remyelination failure after white matter stroke and stimulates functional recovery in aged mice. *Proc. Natl Acad. Sci. USA* **113**, E8453–E8462 (2016).
- Martínez-Lapiscina, E. H. et al. The visual pathway as a model to understand brain damage in multiple sclerosis. *Mult. Scler.* **20**, 1678–1685 (2014).
- Cardin, J. A., Kumbhani, R. D., Contreras, D. & Palmer, L. A. Cellular Mechanisms of Temporal Sensitivity in Visual Cortex Neurons. *J. Neurosci.* **30**, 3652–3662 (2010).
- Denman, D. J. & Reid, R. C. Synergistic population encoding and precise coordinated variability across interlaminar ensembles in the early visual system. *BioRxiv* 812859 (2019).

32. Fries, P., Neuenschwander, S., Engel, A. K., Goebel, R. & Singer, W. Rapid feature selective neuronal synchronization through correlated latency shifting. *Nat. Neurosci.* **4**, 194–200 (2001).
33. Gur, M., Beylin, A. & Snodderly, D. M. Response Variability of Neurons in Primary Visual Cortex (V1) of Alert Monkeys. *J. Neurosci.* **17**, 2914–2920 (1997).
34. Ohiorhenuan, I. E. et al. Sparse coding and high-order correlations in fine-scale cortical networks. *Nature* **466**, 617–621 (2010).
35. Zandvakili, A. & Kohn, A. Coordinated Neuronal Activity Enhances Corticocortical Communication. *Neuron* **87**, 827–839 (2015).
36. Marenga, S. et al. Visual Evoked Potentials to Monitor Myelin Cuprizone-Induced Functional Changes. *Front. Neurosci.* **16**, 820155 (2022).
37. Green, A. J. et al. Clemastine fumarate as a remyelinating therapy for multiple sclerosis (ReBUILD): a randomised, controlled, double-blind, crossover trial. *Lancet* **390**, 2481–2489 (2017).
38. Alshowaier, D. et al. Latency of multifocal visual evoked potentials in nonoptic neuritis eyes of multiple sclerosis patients associated with optic radiation lesions. *Invest Ophthalmol. Vis. Sci.* **55**, 3758–3764 (2014).
39. Morgan, M. L. et al. Cuprizone-induced Demyelination in Mouse Brain is not due to Depletion of Copper. *ASN Neuro* **14**, 17590914221126367 (2022).
40. Zirngibl, M., Assinck, P., Sizov, A., Caprariello, A. V. & Plemel, J. R. Oligodendrocyte death and myelin loss in the cuprizone model: an updated overview of the intrinsic and extrinsic causes of cuprizone demyelination. *Mol. Neurodegeneration* **17**, 34 (2022).
41. Hughes, E. G., Orthmann-Murphy, J. L., Langseth, A. J. & Bergles, D. E. Myelin remodeling through experience-dependent oligodendrogenesis in the adult somatosensory cortex. *Nat. Neurosci.* **21**, 696–706 (2018).
42. Orthmann-Murphy, J. et al. Remyelination alters the pattern of myelin in the cerebral cortex. *eLife* **9**, e56621 (2020).
43. Wang, F. et al. Myelin degeneration and diminished myelin renewal contribute to age-related deficits in memory. *Nat. Neurosci.* **23**, 481–486 (2020).
44. Snaidero, N. et al. Myelin replacement triggered by single-cell demyelination in mouse cortex. *Nat. Commun.* **11**, 4901 (2020).
45. Koening, M. et al. Myelin gene regulatory factor is required for maintenance of myelin and mature oligodendrocyte identity in the adult CNS. *J. Neurosci.* **32**, 12528–12542 (2012).
46. Patrikios, P. et al. Remyelination is extensive in a subset of multiple sclerosis patients. *Brain* **129**, 3165–3172 (2006).
47. Frischer, J. M. et al. Clinical and pathological insights into the dynamic nature of the white matter multiple sclerosis plaque. *Ann. Neurol.* **78**, 710–721 (2015).
48. Baxi, E. G. et al. A selective thyroid hormone  $\beta$  receptor agonist enhances human and rodent oligodendrocyte differentiation. *Glia* **62**, 1513–1529 (2014).
49. Bhat, N. R., Sarlieve, L. L., Rao, G. S. & Pieringer, R. A. Investigations on myelination in vitro. Regulation by thyroid hormone in cultures of dissociated brain cells from embryonic mice. *J. Biol. Chem.* **254**, 9342–9344 (1979).
50. Barres, B. A., Lazar, M. A. & Raff, M. C. A novel role for thyroid hormone, glucocorticoids and retinoic acid in timing oligodendrocyte development. *Development* **120**, 1097–1108 (1994).
51. Hartley, M. D. et al. Myelin repair stimulated by CNS-selective thyroid hormone action. *JCI Insight* **4**, e126329 (2019).
52. Fernandez, M. et al. Thyroid hormone administration enhances remyelination in chronic demyelinating inflammatory disease. *Proc. Natl Acad. Sci. USA* **101**, 16363–16368 (2004).
53. Calza, L., Fernandez, M., Giuliani, A., Aloe, L. & Giardino, L. Thyroid hormone activates oligodendrocyte precursors and increases a myelin-forming protein and NGF content in the spinal cord during experimental allergic encephalomyelitis. *Proc. Natl Acad. Sci. USA* **99**, 3258–3263 (2002).
54. Franco, P. G., Silvestroff, L., Soto, E. F. & Pasquini, J. M. Thyroid hormones promote differentiation of oligodendrocyte progenitor cells and improve remyelination after cuprizone-induced demyelination. *Exp. Neurol.* **212**, 458–467 (2008).
55. Zhang, M. et al. Thyroid hormone alleviates demyelination induced by cuprizone through its role in remyelination during the remission period. *Exp. Biol. Med (Maywood)* **240**, 1183–1196 (2015).
56. Meinig, J. M. et al. Targeting Fatty-Acid Amide Hydrolase with Prodrugs for CNS-Selective Therapy. *ACS Chem. Neurosci.* **8**, 2468–2476 (2017).
57. Chaudhary, P. et al. Thyroid hormone and thyromimetics inhibit myelin and axonal degeneration and oligodendrocyte loss in EAE. *J. Neuroimmunol.* **352**, 577468 (2021).
58. Mei, F. et al. Micropillar arrays as a high-throughput screening platform for therapeutics in multiple sclerosis. *Nat. Med.* **20**, 954–960 (2014).
59. Heidari, M. et al. Evoked potentials as a biomarker of remyelination. *Proc. Natl Acad. Sci.* **116**, 27074–27083 (2019).
60. Halliday, A. M., McDonald, W. I. & Mushin, J. Visual evoked response in diagnosis of multiple sclerosis. *Br. Med. J.* **4**, 661–664 (1973).
61. Kawamura, A. et al. Chd8 mutation in oligodendrocytes alters microstructure and functional connectivity in the mouse brain. *Mol. Brain* **13**, 160 (2020).
62. Liu, J. et al. Clemastine Enhances Myelination in the Prefrontal Cortex and Rescues Behavioral Changes in Socially Isolated Mice. *J. Neurosci.* **36**, 957–962 (2016).
63. Maas, D. A. et al. Interneuron hypomyelination is associated with cognitive inflexibility in a rat model of schizophrenia. *Nat. Commun.* **11**, 2329 (2020).
64. Phan, B. N. et al. A myelin-related transcriptomic profile is shared by Pitt-Hopkins syndrome models and human autism spectrum disorder. *Nat. Neurosci.* **23**, 375–385 (2020).
65. Sun, Y. et al. Dysmyelination by Oligodendrocyte-Specific Ablation of Ninj2 Contributes to Depressive-Like Behaviors. *Adv. Sci.* **9**, 2103065 (2022).
66. Wolf, N. I., French-Constant, C. & van der Knaap, M. S. Hypomyelinating leukodystrophies — unravelling myelin biology. *Nat. Rev. Neurol.* **17**, 88–103 (2021).
67. Kuhlmann, T. et al. Differentiation block of oligodendroglial progenitor cells as a cause for remyelination failure in chronic multiple sclerosis. *Brain* **131**, 1749–1758 (2008).
68. El Behi, M. et al. Adaptive human immunity drives remyelination in a mouse model of demyelination. *Brain* **140**, 967–980 (2017).
69. Karamita, M. et al. Therapeutic inhibition of soluble brain TNF promotes remyelination by increasing myelin phagocytosis by microglia. *JCI Insight* **2**, e87455 (2017). 87455.
70. Trebst, C. et al. Lack of interferon-beta leads to accelerated remyelination in a toxic model of central nervous system demyelination. *Acta Neuropathol.* **114**, 587–596 (2007).
71. Kotter, M. R., Li, W.-W., Zhao, C. & Franklin, R. J. M. Myelin impairs CNS remyelination by inhibiting oligodendrocyte precursor cell differentiation. *J. Neurosci.* **26**, 328–332 (2006).
72. Back, S. A. et al. Hyaluronan accumulates in demyelinated lesions and inhibits oligodendrocyte progenitor maturation. *Nat. Med.* **11**, 966–972 (2005).
73. Cunniffe, N. & Coles, A. Promoting remyelination in multiple sclerosis. *J. Neurol.* **268**, 30–44 (2021).
74. Elbers, L. P. B., Kastelein, J. J. P. & Sjouke, B. Thyroid Hormone Mimetics: the Past, Current Status and Future Challenges. *Curr. Atheroscler. Rep.* **18**, 14 (2016).
75. Schran, H. F., Petryk, L., Chang, C. T., O'Connor, R. & Gelbert, M. B. The pharmacokinetics and bioavailability of clemastine and

- phenylpropanolamine in single-component and combination formulations. *J. Clin. Pharm.* **36**, 911–922 (1996).
76. Törneke, K. et al. Pharmacokinetics and pharmacodynamics of clemastine in healthy horses. *J. Vet. Pharmacol. Therapeutics* **26**, 151–157 (2003).
  77. Hughes, E. G., Kang, S. H., Fukaya, M. & Bergles, D. E. Oligodendrocyte progenitors balance growth with self-repulsion to achieve homeostasis in the adult brain. *Nat. Neurosci.* **16**, 668–676 (2013).
  78. Marisca, R. et al. Functionally distinct subgroups of oligodendrocyte precursor cells integrate neural activity and execute myelin formation. *Nat. Neurosci.* **23**, 363–374 (2020).
  79. Thornton, M. A. et al. Long-term in vivo three-photon imaging reveals region-specific differences in healthy and regenerative oligodendrogenesis. *Nat. Neurosci.* **27**, 846–861 (2024).
  80. Dedoni, S. et al. An overall view of the most common experimental models for multiple sclerosis. *Neurobiol. Dis.* **184**, 106230 (2023).
  81. Reich, D. S., Lucchinetti, C. F. & Calabresi, P. A. Multiple Sclerosis. *N. Engl. J. Med.* **378**, 169–180 (2018).
  82. Thomson, A. M. & Lamy, C. Functional maps of neocortical local circuitry. *Front Neurosci.* **1**, 19–42 (2007).
  83. Yao, S. et al. A whole-brain monosynaptic input connectome to neuron classes in mouse visual cortex. *Nat. Neurosci.* **26**, 350–364 (2023).
  84. Burkhalter, A., Ji, W., Meier, A. M. & D'Souza, R. D. Modular horizontal network within mouse primary visual cortex. *Front Neuroanat.* **18**, 1364675 (2024).
  85. Peng, H. et al. Morphological diversity of single neurons in molecularly defined cell types. *Nature* **598**, 174–181 (2021).
  86. Dustman, R. E. & Beck, E. C. Long-Term Stability of Visually Evoked Potentials in Man. *Science* **142**, 1480–1481 (1963).
  87. Urbach, D., Gur, M., Pratt, H. & Peled, R. Time domain analysis of VEPs. Detection of waveform abnormalities in multiple sclerosis. *Investigative Ophthalmol. Vis. Sci.* **27**, 1379–1384 (1986).
  88. Das, A. et al. Reversible Loss of Hippocampal Function in a Mouse Model of Demyelination/Remyelination. *Front. Cell. Neurosci.* **13**, 588 (2020).
  89. Auer, F., Vagionitis, S. & Czopka, T. Evidence for Myelin Sheath Remodeling in the CNS Revealed by In Vivo Imaging. *Curr. Biol.* **28**, 549–559.e3 (2018).
  90. Snaidero, N. et al. Myelin membrane wrapping of CNS axons by PI(3,4,5)P<sub>3</sub>-dependent polarized growth at the inner tongue. *Cell* **156**, 277–290 (2014).
  91. Dupree, J. L. et al. Oligodendrocytes assist in the maintenance of sodium channel clusters independent of the myelin sheath. *Neuron Glia Biol.* **1**, 179–192 (2004).
  92. Ramaglia, V. et al. Complement-associated loss of CA2 inhibitory synapses in the demyelinated hippocampus impairs memory. *Acta Neuropathol.* **142**, 643–667 (2021).
  93. Araújo, S. E. S. et al. Inflammatory demyelination alters subcortical visual circuits. *J. Neuroinflammation* **14**, 162 (2017).
  94. Dubey, M. et al. Myelination synchronizes cortical oscillations by consolidating parvalbumin-mediated phasic inhibition. *eLife* **11**, e73827 (2022).
  95. Crawford, D. K., Mangiardi, M., Xia, X., López-Valdés, H. E. & Tiwari-Woodruff, S. K. Functional recovery of callosal axons following demyelination: a critical window. *Neuroscience* **164**, 1407–1421 (2009).
  96. Gong, S. et al. A gene expression atlas of the central nervous system based on bacterial artificial chromosomes. *Nature* **425**, 917–925 (2003).
  97. Schindelin, J. et al. Fiji: an open-source platform for biological-image analysis. *Nat. Methods* **9**, 676–682 (2012).
  98. Berg, S. et al. ilastik: interactive machine learning for (bio)image analysis. *Nat. Methods* **16**, 1226–1232 (2019).
  99. Ollion, J., Cochennec, J., Loll, F., Escudé, C. & Boudier, T. TANGO: a generic tool for high-throughput 3D image analysis for studying nuclear organization. *Bioinformatics* **29**, 1840–1841 (2013).
  100. Parslow, A., Cardona, A. & Bryson-Richardson, R. J. Sample drift correction following 4D confocal time-lapse imaging. *J. Vis. Exp.* **86**, 51086 (2014).
  101. Matsumoto, A. et al. Direction selectivity in retinal bipolar cell axon terminals. *Neuron* **109**, 2928–2942.e8 (2021).
  102. Jun, J. J. et al. Fully integrated silicon probes for high-density recording of neural activity. *Nature* **551**, 232–236 (2017).

## Acknowledgements

We thank Laboratory Animal Resources at CU Anschutz for assistance with mouse drug treatments and PW Hosokawa for statistical consulting. Michael Liebling developed the PoorMan3D registration plugin for ImageJ. This work was funded by the following sources: Sponsored research agreement with Autobahn Therapeutics Inc. (E.G.H., D.J.D.), National Institutes of Health grants NS115975, NS125230, NS132859, NS134829 (E.G.H.) and NS120850, EY028612 (D.J.D.). National Multiple Sclerosis Society Postdoctoral Fellowships FG-2208-40305 (L.A.O.) and FG-2107-38324 (G.D.F.N.). Department of Defense Multiple Sclerosis Research Program Early Investigator Research Award HT9425-23-1-0561 (L.A.O.).

## Author contributions

D.J.D., E.G.H., G.D.F.N., L.A.O., R.G., J.A.V. conceived the project. L.A.O. and G.D.F.N. wrote the original manuscript, administered the project execution, performed experiments (surgeries, drug treatment, in vivo imaging), carried out in vivo image analysis and all statistical analysis, and created all figures. J.A.H. performed pilot experiments and collected part of the samples for histology. L.C. performed part of the in vivo imaging and in vivo imaging analysis. M.A.T. performed surgeries and part of the confocal imaging reported in Supplementary Fig. 9. M.E.S. performed surgeries. K.A.B., A.M., and G.D.F.N. performed immunohistochemistry, confocal imaging, and analysis that are reported in Supplementary Figs. 1, 2C–E, and 9. J.A.G. carried out the immunohistochemistry of the retina reported in Supplementary Fig. 2A, B and was supervised by A.P.-P.; Y.I.M.C. carried out part of the in vivo imaging analysis. A.R.C. performed mouse husbandry and genotyping. A.R.C. and A.M. sectioned the optic nerve and brain tissue. M.B.W., D.A.M., and A.A. facilitated the gene expression analysis reported in Supplementary Fig. 6E–H. D.A.M. facilitated the analysis of thyroid hormone receptor selectivity in Supplementary Fig. 6A. A.D. facilitated the OPC differentiation experiment reported in Supplementary Fig. 6B–D. D.J.D. performed and analyzed the electrophysiology experiments reported in Figs. 6, 7, Supplementary Figs. 12–15. D.J.D., E.G.H., R.G. and J.A.V. formulated the initial Sponsored Research Agreement. D.J.D. and E.G.H. supervised the project. G.D.F.N., L.A.O., D.J.D., E.G.H., J.A.V., and DAM revised and edited the manuscript.

## Competing interests

M.B.W., D.A.M., A.A., A.D., J.A.V., and R.G. were employees of Autobahn Therapeutics and hold equity interests in the company. J.A.V. remains an employee of Autobahn Therapeutics. Autobahn Therapeutics developed LL-341070 and provided LL-341070 for experiments. In vitro data and rat gene expression data (Supplementary Fig. 6) were provided by Autobahn Therapeutics. This project was funded in part by a Sponsored Research Agreement between Autobahn Therapeutics and E.G.H. and D.J.D.; academic freedom was maintained in designing and analyzing experiments and in writing the manuscript. All other authors have no other current or past financial involvements with Autobahn Therapeutics, or other competing interests to declare.

## Additional information

**Supplementary information** The online version contains supplementary material available at <https://doi.org/10.1038/s41467-025-56092-6>.

**Correspondence** and requests for materials should be addressed to Daniel J. Denman or Ethan G. Hughes.

**Peer review information** *Nature Communications* thanks Peter Calabresi, who co-reviewed with Marjan Gharagozloo and the other, anonymous, reviewers for their contribution to the peer review of this work. A peer review file is available.










**Reprints and permissions information** is available at <http://www.nature.com/reprints>

**Publisher's note** Springer Nature remains neutral with regard to jurisdictional claims in published maps and institutional affiliations.

**Open Access** This article is licensed under a Creative Commons Attribution-NonCommercial-NoDerivatives 4.0 International License, which permits any non-commercial use, sharing, distribution and reproduction in any medium or format, as long as you give appropriate credit to the original author(s) and the source, provide a link to the Creative Commons licence, and indicate if you modified the licensed material. You do not have permission under this licence to share adapted material derived from this article or parts of it. The images or other third party material in this article are included in the article's Creative Commons licence, unless indicated otherwise in a credit line to the material. If material is not included in the article's Creative Commons licence and your intended use is not permitted by statutory regulation or exceeds the permitted use, you will need to obtain permission directly from the copyright holder. To view a copy of this licence, visit <http://creativecommons.org/licenses/by-nc-nd/4.0/>.

© The Author(s) 2025

---

**Gustavo Della-Flora Nunes** <sup>1,4</sup>, **Lindsay A. Osso** <sup>1,4</sup>, **Johana A. Haynes**<sup>1</sup>, **Lauren Conant**<sup>1</sup>, **Michael A. Thornton**<sup>1</sup>, **Michael E. Stockton** <sup>1</sup>, **Katherine A. Brassell** <sup>1</sup>, **Amanda Morris**<sup>1</sup>, **Yessenia I. Mancha Corchado**<sup>1</sup>, **John A. Gaynes**<sup>2</sup>, **Anthony R. Chavez**<sup>1</sup>, **Michaelanne B. Woerner**<sup>3</sup>, **Deidre A. MacKenna**<sup>3</sup>, **Aryan Alavi**<sup>3</sup>, **Anne Danks**<sup>3</sup>, **Alon Poleg-Polsky** <sup>2</sup>, **Rohan Gandhi**<sup>3</sup>, **Jeffrey A. Vivian**<sup>3</sup>, **Daniel J. Denman** <sup>2,5</sup>  & **Ethan G. Hughes** <sup>1,5</sup> 

---

<sup>1</sup>Department of Cell and Developmental Biology, University of Colorado School of Medicine, Aurora, CO, USA. <sup>2</sup>Department of Physiology and Biophysics, University of Colorado School of Medicine, Aurora, CO, USA. <sup>3</sup>Autobahn Therapeutics Inc, San Diego, CA, USA. <sup>4</sup>These authors contributed equally: Gustavo Della-Flora Nunes, Lindsay A. Osso. <sup>5</sup>These authors jointly supervised this work: Daniel J. Denman, Ethan G. Hughes.

 e-mail: [daniel.denman@cuanschutz.edu](mailto:daniel.denman@cuanschutz.edu); [ethan.hughes@cuanschutz.edu](mailto:ethan.hughes@cuanschutz.edu)